Renewable Energy 212 (2023) 17–34

Contents lists available at ScienceDirect

Renewable Energy

journal homepage: www.elsevier.com/locate/renene

Experimental study of the turbulent flow in the wake of a horizontal axis tidal current turbine

Fabio Di Felice [a], Alessandro Capone [a], Giovanni Paolo Romano [b], Francisco Alves Pereira [a,*]

[a] Institute of Marine Engineering, National Research Council (CNR-INM), Via di Vallerano 139, 00128 Rome, Italy
[b] Dept. Mechanical & Aerospace Engineering, University "La Sapienza", Via Eudossiana 18, 00184 Rome, Italy

ARTICLE INFO

Keywords:
Ocean tidal energy
Horizontal axis tidal current turbine
Tidal turbine performance
In-phase velocity field
Turbulent kinetic energy
Particle image velocimetry (PIV)

ABSTRACT

A scaled-model of a horizontal axis tidal current turbine (HATCT) is tested in the CNR-INM Circulating Water Channel. The experiments are designed to establish in the first place the performances of the turbine at different working settings. The second goal is to investigate the hydrodynamics generated by the turbine in the near wake using the Particle Image Velocimetry (PIV) technique. For this purpose, velocity measurements are performed in a longitudinal plane and phase-locked to the rotor angle in order to resolve the wake structure at different working regimes. The analysis of the axial and radial velocity fields reveals the flow features of the slipstream, as well as its expansion and dependence on the turbine operating parameters. Analysis of the non-diagonal terms of the Reynolds stress tensor provides insight into the onset of tip vortex pairing and of vortex instabilities. Furthermore the separate contributions of transport, production and dissipation to the turbulent kinetic energy in the wake field are discussed in detail. The vortex unsteadiness is captured and correlated with the evolution of the kinetic energy transport and production terms. Understanding these phenomenologies is an important step to develop computational tools able to estimate the radiated noise or the potential impact of turbulence on performances of further rotors placed in the wake, as in an array of tidal turbines.

1. Introduction

1.1. Tidal resources in the energy economy

Energy supply is at the heart of the struggle against global warming, with power plants accounting for about 30% of all carbon dioxide released per unit of electricity production. In 2022, the European Commission launched the Horizon Europe program in the wake of the Green Deal. A clear and ambitious objective was set to target a sustainable, resource-efficient and competitive economy with at least 55% of greenhouse gas (GHG) emission reduction by 2030 compared to 1990 and no net emission of GHG by 2050. Climate, Energy and Mobility are amongst the most important actions of the program with a budget of €15,3 bn out of a €53,5 bn planned for global challenges and European competitiveness.

In that context, tidal current energy is one of the most attractive renewable and clean energy resources for electricity generation and is expected to expand significantly in the near future. One distinct advantage over other renewable energy sources lays in its regular and foreseeable nature. In fact tidal streams are entirely predictable since they stem from the constant and periodic motion of the sea water body under the action of the gravitational forces exerted by the Moon and Sun upon the rotating Earth. Thanks to this high predictability, tidal technologies are regarded as a major asset for the electrical grid in terms of competitiveness and energy output potential, along with a low impact on the environment, social acceptance and a strong prospect to create industrial activity.

1.2. Understanding the hydrodynamics of tidal turbines

The extensive studies on wind turbines carried out over the last decades, starting from the seminal work by [1], can be generally extended to marine tidal turbines. Nevertheless a major difference arises for the latter because of the interaction with the free surface or the seabed. For instance, the presence of strong vortical structures in the wake of the rotor can induce erosion and interfere with the natural mechanisms of sediment transport by the marine currents in the installation site. As such, scientific research on horizontal axis tidal turbines has experienced in the past decade a strong impulse towards a better understanding of the interactions with the surrounding environment, alongside new solutions for performance improvement. In

* Corresponding author.
E-mail addresses: fabio.difelice@cnr.it (F. Di Felice), alessandro.capone@cnr.it (A. Capone), giampaolo.romano@uniroma1.it (G.P. Romano), francisco.alvespereira@cnr.it (F. Alves Pereira).

https://doi.org/10.1016/j.renene.2023.04.128
Received 4 July 2022; Received in revised form 1 March 2023; Accepted 26 April 2023
Available online 3 May 2023

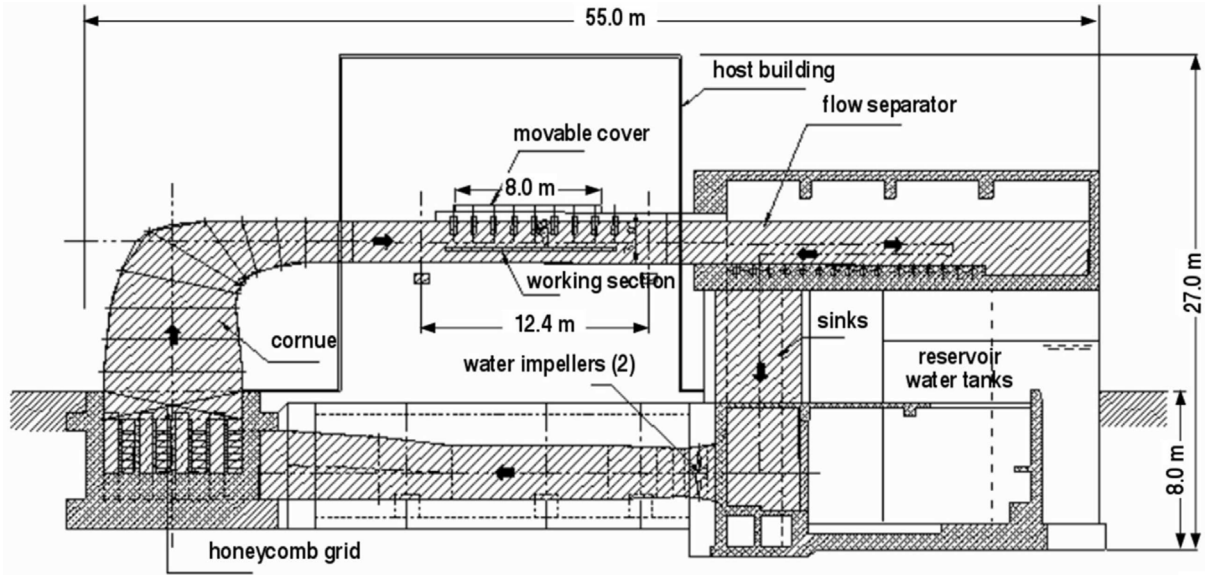

Fig. 1. Schematic view of the CNR-INM circulating water channel.

this regard, several research studies have focused on the measurement and prediction of global quantities such as thrust and torque, and their dependence on the hydrodynamic conditions [2–5]. For the purpose of maximizing energy extraction, multiple turbines are normally distributed into arrays, or tidal farms. Therefore, the knowledge and understanding of the flow structures developing in the wake of a single tidal turbine can play a key role as flow perturbations may affect the performances of neighboring turbines and, possibly, of the turbine farm system as a whole.

In an early work [6], the wake induced by a 1:34 scaled marine current turbine was investigated by pitot tube and water surface elevation measurements. Concurrently, non-intrusive velocimetry techniques such as Laser Doppler Velocimetry (LDV) and Acoustic Doppler Velocimetry (ADV) were being increasingly used over the years by researchers, in particular in the fields of wind turbine aerodynamics and naval hydrodynamics, and are being slowly introduced in the field of marine turbines. A 3-blade tidal turbine was studied in [7] via LDV to investigate the effect of the inflow properties, e.g. turbulence and yaw angle, on the mean and turbulent flow characteristics of the rotor wake. ADV was employed to analyze the far wake of a rotor by simulating the turbine as a porous disk in [8]. In another work [9], the spectral features of the wake of a three-blade horizontal turbine in an open channel flow were analyzed via ADV. It was shown that the instantaneous power generated by a marine turbine is strongly coupled with the energy cascade of the flow in the low-frequency region, below the turbine rotational frequency. Low-frequency wake meandering was also observed at distances greater than three rotor diameters, with a dominant frequency obeying a Strouhal number of 0.28. Near and far-field perturbations in the wake of a single model turbine were studied in [10] by analyzing the vertical and longitudinal velocity profiles obtained via ADV. The work described in [11] reports the results of an experimental campaign carried out by phase-locked LDV measurements in the wake generated by a six-blade horizontal axis tidal turbine at different blade tip speed ratios. It was shown that up to 8% of the inflow energy is converted in cross-flow components' energy. More recently in [12,13], ADV was employed to provide an average three-dimensional representation of a three-blade turbine wake up to 20 rotor diameters downstream, along with visualizations of the instantaneous wake structures. Effects of blockage and of bypass flow on the formation of the wake of a three-blade turbine were investigated via ADV by [14]. Large eddy simulations (LES) of the flow structure in the wake of a commercial horizontal axis tidal turbine are described in [15] whereas Reynolds Averaged Navier–Stokes (RANS) simulations were employed in [16] to look at the performance of diffuser-augmented tidal current turbine. Recently, multiple turbine arrangements were investigated by LES in [17,18] who reported substantial modifications in the wake structure of neighboring turbines due to the inflow perturbation, compared to an isolated turbine configuration. A recent experimental work [19] looked at the effect of longitudinal and lateral spacing in a staggered 4-rotor array operated in a shallow water channel. Results are made in terms of velocity deficit, outlining in particular that the downstream turbines should be tuned to the locally altered inflow conditions in order to be operated at maximum efficiency.

1.3. Rationale of the proposed work

The studies reviewed thus far provide useful grounds for analysis and design. Understanding the wake structure in detail and identifying different flow mechanisms can provide insight into improving rotor design from a hydrodynamic perspective. For example, blade load distribution can be inferred from the trailing edge vorticity, and improvements can be made in terms of section thickness or chord length distribution. The vortex behavior is a central player in the kinetic energy recovery process, which is important for optimizing the tidal array deployment. In fact inducing vortex instability at short distance from the rotor plane helps to accelerate the recovery of the flow kinetic energy behind the turbine and maximize the energy input for the next rotor. Understanding its evolution in the rotor wake is also important to address the problem of seabed erosion.

However the unsteady and periodic nature of the wake is not yet fully uncovered nor understood. To date, the baseline experimental approach has been to analyze turbine hydrodynamics in terms of macroscopic quantities, specifically time-averaged velocity data, resulting in a simplified description of the physical phenomena and a limited understanding of their impact on performance. The flow released by the rotor in the near wake is characterized by strong, periodic, coherent flow structures at the blade tip and hub vortices [11], which are convected downstream and undergo complex mechanisms of destabilization eventually leading to their breakdown. This has been well documented in the case of wind turbine wakes [20–24]. Additionally, several experimental and numerical analyses have demonstrated the link between the momentum deficit in the turbine wake and rotor performance. Still, an accurate prediction of the wake characteristics such as recovery length and expansion rate is difficult, especially for

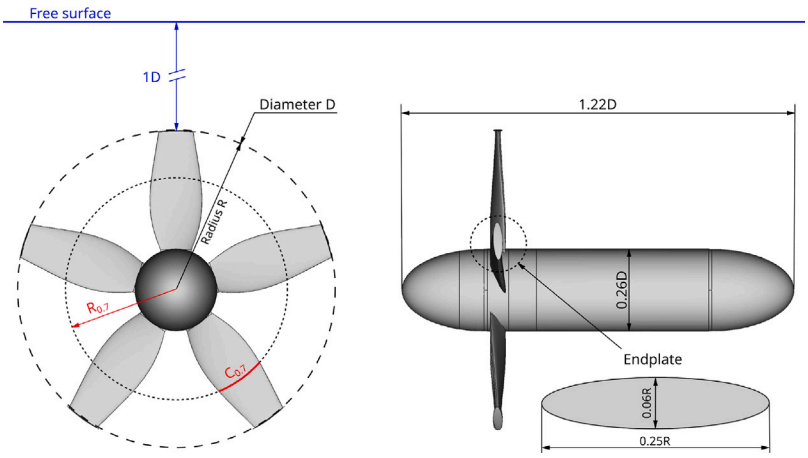

Fig. 2. Dimensional characteristics of the 5-blade horizontal axis tidal current tidal turbine model.

farm deployments where multiple wakes are produced by clusters of turbine rotors. The large inaccuracies in the numerical analysis of the kinetic energy recovery are typically associated with a poor modeling of the wake and turbine loads, typically based on actuator disk or actuator line models as shown in [25]. Accurate and detailed experimental data is still needed to support the development of realistic computational models.

1.4. Objectives and approach

The introduction of non-intrusive measurement techniques in recent years has allowed a powerful description of rotor wakes. Particle Image Velocimetry, hereafter PIV, has been used extensively for wind turbine wake studies [23,26–28] providing an accurate description of the downstream evolution of the wake. To the authors' knowledge, very few studies provide such a description in the case of tidal turbines, or provide only an average view of the wake flow [19]. As a matter of fact a detailed description of flow structures developing in the wake of such devices is still needed for the development of theoretical models and computational tools. In this work we build upon this knowledge to analyze the wake development of a five-blade tidal turbine, using in-phase PIV in a longitudinal plane down to one diameter into the rotor wake. The phase-locked approach used here allows to investigate in detail the flow topology and statistics in correlation with the turbine performance. The main flow characteristics are discussed in connection with the operating working conditions of the turbine so as to shed light onto the interactions between turbine power settings and wake features such as blade wake, tip and hub vortex evolution and slipstream expansion. The discussion finally introduces several physical considerations in terms of turbulent kinetic energy and its development in the rotor wake.

2. Experimental methodology

2.1. Test facility

The experiment is performed in the CNR-INM circulating water channel, a free surface cavitation channel with a test section of 3.6 m in width, 2.25 m in depth from free surface to bottom, and 12.4 m in length, see Fig. 1. The tunnel can reach a flow velocity of 5.2 m s^{-1} and the pressure can be reduced to a minimum of 40 mbar to simulate a range of full scale cavitation numbers. The freestream turbulence in the test section is 2.5% of the mean inflow velocity and the velocity flow uniformity is within 1% across the section.

2.2. Turbine model

The model used in the experimental study is a 5-blade, horizontal axis tidal current turbine model with a diameter $D = 500$ mm, see Fig. 2 for the dimensional description. The main characteristic of the turbine lays in the symmetrical blade sections, which make possible to work both with the ebb and flow phases of the tidal cycle without requiring any yaw alignment device on the rotor. To allow this two-way operation, the blade sections have an elliptical shape with a maximum thickness equal to 16% of the chord length. The chord distribution is variable along the span with a maximum length at $r/R = 0.55$, with $R = D/2$ being the rotor radius. The blades are equipped with tip endplates to delay the tip vortex formation and reduce the hydrodynamic losses caused by the pressure drop between the face and the back of the blade in the tip region. The geometry of the endplates follows the elliptical cross-section of the blade, see Fig. 2.

Fig. 3 shows the actual rotor installed in the test section. The rotor axis is placed at $1.5D$ below the free surface and the tip immersion depth is $1D$, see Fig. 2. The turbine is installed on a Kempf & Remmers dynamometric force balance. The dynamometer allows to measure the thrust T, the torque Q, and the forces along 3 axes. The turbine is put in rotation by a 15 kW brushless motor and the control of the rotational speed is done with high accuracy by a dedicated power and control unit.

2.3. Velocimetry measurements

Flow velocity is measured by means of a two-dimensional Particle Image Velocimetry (2D PIV) system consisting of a double-cavity 200 mJ Nd-YAG laser and a double shutter camera with a resolution of 4000 × 2672 pixels. The sketch of the instrumentation set-up is shown in Fig. 4. An encoder is mounted on the dynamometer shaft and feeds the angular position to a signal processor with a resolution of 0.1°. Once per rotor revolution, a pulse signal is sent to a synchronizing device, which in turn provides an adequately delayed sequence of TTL signals to the camera and laser components of the PIV system, in order to allow image acquisitions that are thus phased-locked with the rotor angular position. PIV image pairs are recorded by the camera at a frame rate of 4 Hz. The temporal distance between the two images of the pair is set to 200 μs.

The instantaneous velocity fields are acquired from a distance of 1800 mm from the side window of the test section. Using a lens with a 105 mm focal length and a 2.8 f-number aperture setting, the imaged area is approximately 340 × 450 mm^2. The laser light sheet is delivered in the measurement plane through a glass window placed at the bottom

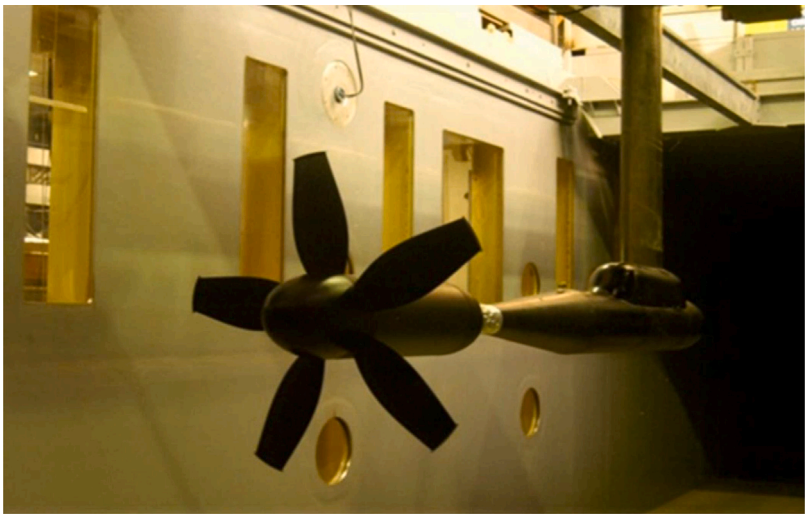

Fig. 3. Turbine model installed on the dynamometer in the test section of the facility.

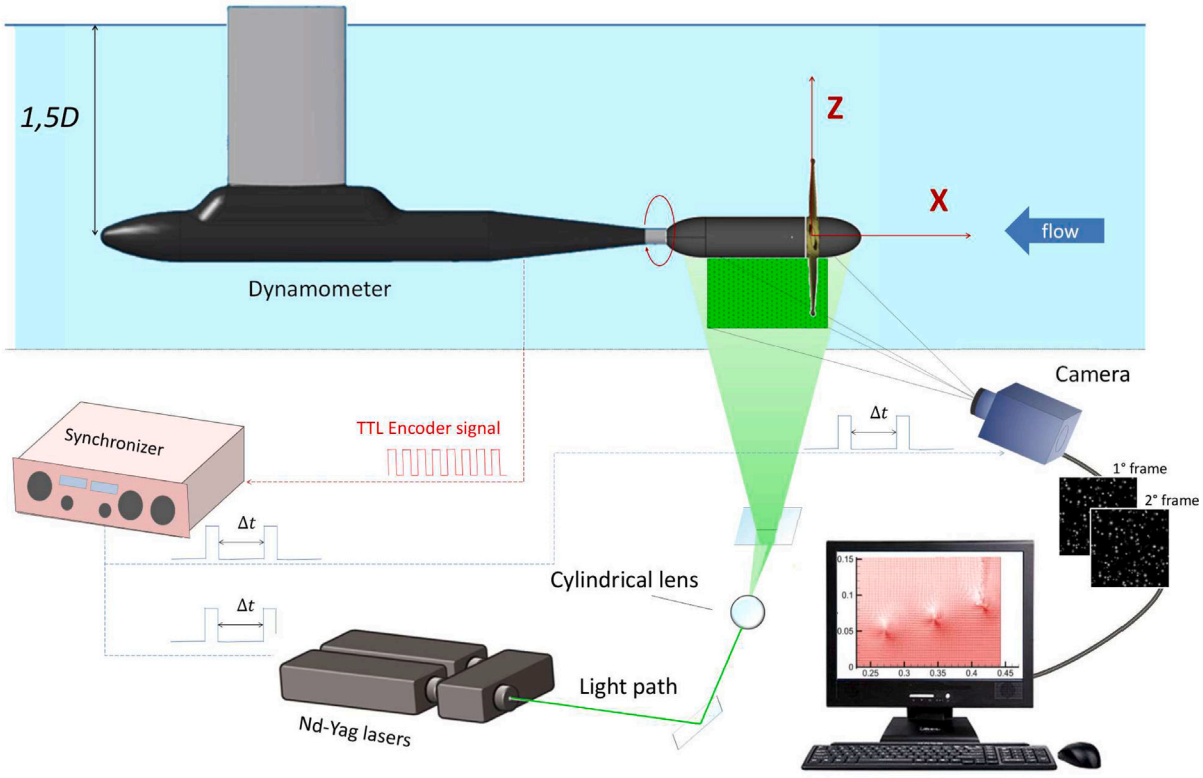

Fig. 4. Schematic view of the experimental setup.

of the facility and is approximately 2 mm thick in the measurement location.

Adequate tracer particles must be chosen in order to accurately follow the water flow [29]. Furthermore, homogeneous dispersion of the seeding particles is a critical aspect in order to reach an uniform distribution within the test channel as well as sufficient seeding density for optimal performance of the PIV cross-correlation algorithm [29]. Based on expertise gained from previous experiments, the water in the tunnel is seeded with 10 μm hollow glass spherical particles, silver-coated for high reflectivity and a mean density of about 1 g mm^{-3} ± 5%. The particle relaxation time is approximately 1×10^{-5} s and is about four orders of magnitude smaller than the time between two blade passages, which is taken as the characteristic time. Hence the selected seeding particles are adequate flow tracers that do not affect the flow and follow accurately the fluid motion [30].

To improve the accuracy and minimize the number of spurious vectors typically present after a PIV analysis, the images are pre-processed by subtracting the minimum background image obtained from the complete image dataset. This procedure helps to reduce the effect of light reflections from the nacelle and the rotor blades. The resulting images are then analyzed using a PIV algorithm combining a discrete offset technique and an iterative image deformation method [31]. In this process, the displacement field obtained with the first analysis step is used to distort the images, upon which direct cross-correlation is applied to calculate the offset-free velocity field. This newly updated velocity predictor is subsequently used to re-distort the

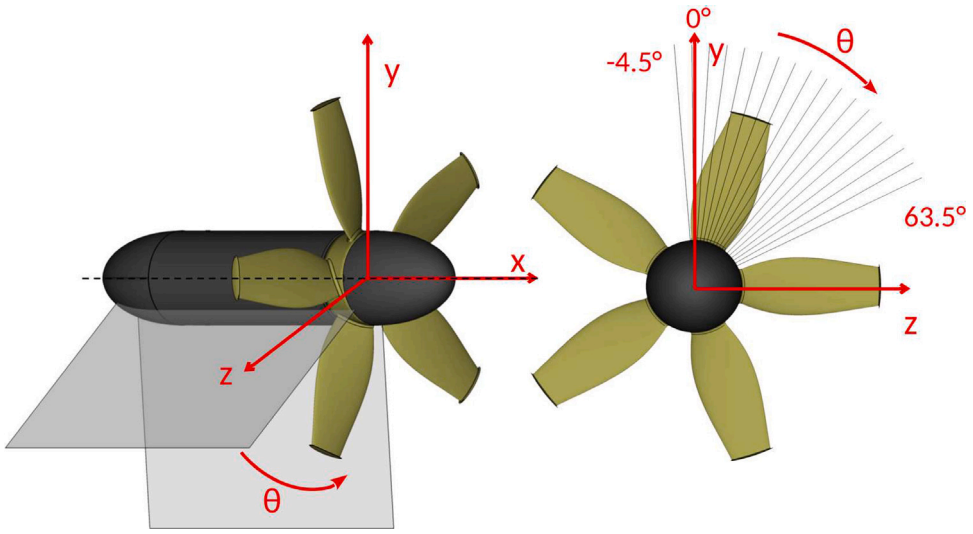

Fig. 5. Reference system of the measurements.

original images and the process is repeated on an iterative basis until a predefined convergence criterion is verified. For the results presented in the following sections, a final window size of 32 × 32 pixels, with 75% overlap between two adjacent windows, is chosen as it offers the best compromise in terms of spurious vector reduction and spatial resolution. The final window size is equivalent to 3.2 mm × 3.2 mm in physical space.

2.4. Phase-locked analysis

Acquisitions are performed in phase with the rotor angular position, spanning from −4.5° to 63.5° with a step of 4°, see Fig. 5 for a description of the reference system. For each angular step 1000 instantaneous measurements are acquired to perform the wake statistical analysis. With this number of instantaneous samples, the convergence of the second order statistical moment is verified. The resulting accuracy for the phase-averaged velocity field is approximately 1% in the regions of higher velocity fluctuations, with a confidence interval of 95% based on the t-Student distribution.

2.5. Operating parameters

The aim of the experimental campaign is to investigate the topology and hydrodynamics of the wake at different working regimes of the turbine, identified by the tip speed ratio (TSR) defined as $\lambda = \omega R/U_\infty$, where ω is the angular velocity of the rotor, R the rotor radius and U_∞ the inflow velocity. The turbine thrust, torque and power coefficients are defined respectively as

$$C_T = \frac{T}{\frac{1}{2}\rho U_\infty^2 A}, \qquad C_Q = \frac{Q}{\frac{1}{2}\rho U_\infty^2 A R}, \qquad C_P = \frac{P}{\frac{1}{2}\rho U_\infty^3 A} = \lambda \cdot C_Q \quad (1)$$

where ρ and $A = \pi R^2$ are the fluid density at the temperature of the water in the facility (17 °C) and the rotor disk area, respectively.

The investigation of the velocity field behind the turbine is conducted through PIV velocity measurements, over a 11 range of operative conditions corresponding to different tip speed ratios λ, see Table 1. The λ values are in the interval 0.60 to 6.50 and allow to cover a variety of operating conditions of interest from rotor stall (low λ) to regimes of maximum torque coefficient C_Q and maximum power coefficient C_P, and further to unloaded operation at higher tip speed ratios λ. Stall is typical of lifting bodies operating at high flow angles of attack. For a turbine this condition appears at low values of λ and a large part of the flow kinetic energy is converted into drag rather than lift and consequently into reduced torque. In contrast to stall, operation at high λ corresponds to very low or even negative angles of attack leading to the unloading of blade sections. In this situation, the incoming kinetic energy passes through the turbine as it is not efficiently used to generate lift and torque. Both stall and unloading conditions are characterized by a drop of the power coefficient, but exhibit two very distinct wake contents later discussed in Section 3.2. Table 1 also reports the Reynolds number $Re_{0.7}$ defined at 70% of the rotor radius, with $Re_{0.7} = U_{0.7}\, C_{0.7}/\nu$ where ν is the water kinematic viscosity at the water temperature, $U_{0.7} = U_\infty \sqrt{1 + (0.7\lambda)^2}$ and $C_{0.7}$ is the chord at radius $R_{0.7} = 0.7R$, see Fig. 2.

For each operating condition listed in Table 1, the dynamics of the wake during the rotor revolution are explored based on the velocity fields recorded via PIV. It must be noted that the small-scale structures of the wake are dependent on both rotor geometry and working conditions; however the flow features at larger scales retain a general validity and relevance in terms of physical understanding and modeling, and the discussion hereafter can be extended to the wake of any tidal turbine.

3. Results and discussion

In the following discussion, we apply the triple Reynolds decomposition $U = \overline{U} + \widetilde{U} + u$, where the flow velocity vector U is the sum of the mean component $\overline{U}$, of the periodic component $\widetilde{U}$ and of the fluctuating part u [32]. We note that the phase-dependent part $\widetilde{U}$ is already accounted for by the mean component $\overline{U}$ since the flow is sampled in a phase-locked manner, such that it is possible to simply write $U = \overline{U} + u$. The axial and radial components of the velocity are identified by the subscripts x and r, i.e. U_x and U_r respectively.

3.1. Turbine performance

The free surface effects can be neglected since the turbine is operated at a tip immersion depth of $1D$, see Fig. 2, where its performance is not affected [4,33,34]. Another consideration regards the possible effect of cavitation on the turbine performance. The cavitation number is defined as $\sigma_{tip} = (p_\infty - p_v)/(\frac{1}{2}\rho U_{tip}^2)$ where p_∞ is the total pressure at the tip immersion depth, p_v is the vapor pressure at the water temperature and $U_{tip} = U_\infty \sqrt{1 + \lambda^2}$ is the tip velocity. Since no cavitation was observed at the most cavitation-prone condition, i.e. at the highest λ where $\sigma_{tip} \approx 0.8$, cavitation has not bearing in the current experiments. The Reynolds number is the governing parameter, see Table 1.

Table 1
Summary of performance tests for the selected 11 operative conditions.

λ	0.60	1.20	1.56	2.00	2.60	2.80	3.00	3.80	4.60	5.50	6.50
$C_T/C_{T_{max}}$	0.64	0.77	0.84	0.90	0.96	0.98	0.99	1.00	0.97	0.89	0.76
$C_Q/C_{Q_{max}}$	0.13	0.19	0.31	0.34	0.37	0.36	0.32	0.24	0.18	0.12	0.04
$C_P/C_{P_{max}}$	0.08	0.23	0.49	0.69	0.97	1.00	0.97	0.92	0.85	0.64	0.26
$Re_{0.7}$ ($\times 10^6$)	0.20	0.24	0.27	0.31	0.38	0.40	0.42	0.52	0.62	0.73	0.85

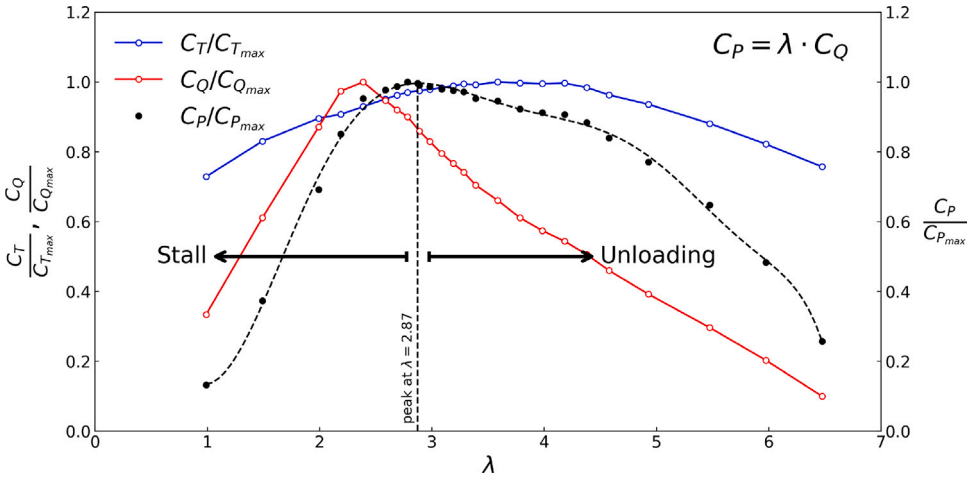

Fig. 6. Turbine performance curves at $U_\infty = 2.51$ m s^{-1}. The dashed line represents a polynomial fit of the power coefficient C_P.

Following the ITTC procedure 7.5-02-07-03.9, a preliminary performance analysis is carried out for λ ranging from 0.0 to 6.50 and for different inflow velocities with the purpose of identifying an asymptotic behavior of the turbine performances with respect to the Reynolds number. From this assessment step, the turbine model performance coefficients are found to increase with inflow velocity with evidence of an asymptotic behavior for inflow speeds above 2.26 m s^{-1}. Performances measured at lower velocities are subject to important viscous and dissipative effects and are not representative of full scale conditions. Upon this preliminary performance analysis, the PIV campaign to investigate the wake flow field is performed at a constant inflow velocity of 2.51 m s^{-1} while the rotational velocity ω is varied to cover the λ values reported in Table 1.

The normalized values of C_T, C_Q and $C_P = \lambda \cdot C_Q$ are shown in Fig. 6 versus λ for $U_\infty = 2.51$ m s^{-1}. We observe how the thrust continues to contribute to the power output of the turbine despite the decreasing trend of torque. However, this contribution quickly vanishes as λ increases and unloading takes place.

3.2. Wake topology

The phase-locked evolution of the mean axial velocity $\overline{U_x}$, non-dimensionalized by the upstream velocity U_∞, is displayed in Video S1 for selected values of λ as per Table 1 and at varying angular positions. Fig. 7 is relative to $\lambda = 3.00$, close to the maximum power coefficient of the turbine. The distribution exhibits an extended region of velocity loss ($\overline{U_x}/U_\infty < 1$) located downstream of the rotor due to the pressure drop caused by the mechanical work of the blades as they extract energy from the inflow, see plot at $\theta = -4.5°$. We also observe the flow acceleration ($\overline{U_x}/U_\infty > 1$) outside the turbine wake tube, caused by the blockage of the turbine rotor and the consequent displacement of the upstream flow in the outward direction. The slipstream boundary between these two distinct regions is delimited by the envelope of the tip vortex traces released by the blades that propagate in the downstream direction, see plot at $\theta = 7.5°$. These traces are recognizable as paired spots of positive and negative axial velocity U_x. Furthermore, a layer of accelerated flow is visible in the vicinity of the nacelle, see plot at $\theta = 7.5°$. In fact, the blade section at the root contributes poorly to loading as the incoming flow is accelerated around the nose body and the tangential velocity is low. As such the incoming flow preserves part of its kinetic energy in this region, creating the higher speed layer.

The tip vortex traces are also identified on the map of the radial velocity shown in Fig. 8 as they are expressed by paired spots of positive and negative $\overline{U_r}$ of similar magnitude, highlighted in the plot at $\theta = -4.5°$ with black circles. Close to the rotor plane, these spots display strong velocity gradients that decay gradually in the downstream direction. Furthermore the highly three-dimensional nature of the flow found at the wall at the intersection between the nacelle and the blades, along with the developing boundary layer over the nacelle, contributes to generate vortical structures that propagate along the nacelle wall. The presence of these flow structures can be evinced in Figs. 7 and 8 in the form of spots located along the nacelle within the accelerated flow layer, with values of the axial and radial velocity following a periodic pattern, see the plot at $\theta = -4.5°$ in Fig. 8.

In order to corroborate these observations, the mean radial and axial components of the velocity field are used to evaluate the mean tangential component of the vorticity $\overline{\omega_\theta}$ defined as

$$\overline{\omega_\theta} = \frac{\partial \overline{U_r}}{\partial x} - \frac{\partial \overline{U_x}}{\partial r} \tag{2}$$

and reported in Fig. 9. The blade tip vortex is outlined as it is convected downstream, see plot at $\theta = 7.5°$. Closer to the rotor, the tip vortex is seen to be the result of a merging process between the twin vortices released by the endplate from the high and low pressure sides of the blade, see the vorticity plots at $\theta = 19.5°$ and $\theta = 31.5°$ and the merged vortex at $\theta = 43.5°$ and $55.5°$. This process is also well observed on the vorticity plot of Video S3. Similarly the pressure gradient along the trailing edge corresponds to a velocity difference between the two sides of the blade, hence forming a shear layer recognizable by the marked vorticity trails seen in Fig. 9 and highlighted on the plot at $\theta = 55.5°$. Furthermore, the presence of the root vortices traveling along the nacelle is now clearly outlined, see plot at $\theta = 55.5°$.

In the downstream section of the wake, the intensity, size and shape of the mean tip vorticity spots associated to the tip vortex undergo strong transformations. We note that the peak intensity of the tip vorticity decays in the downstream direction, as also inferred from the

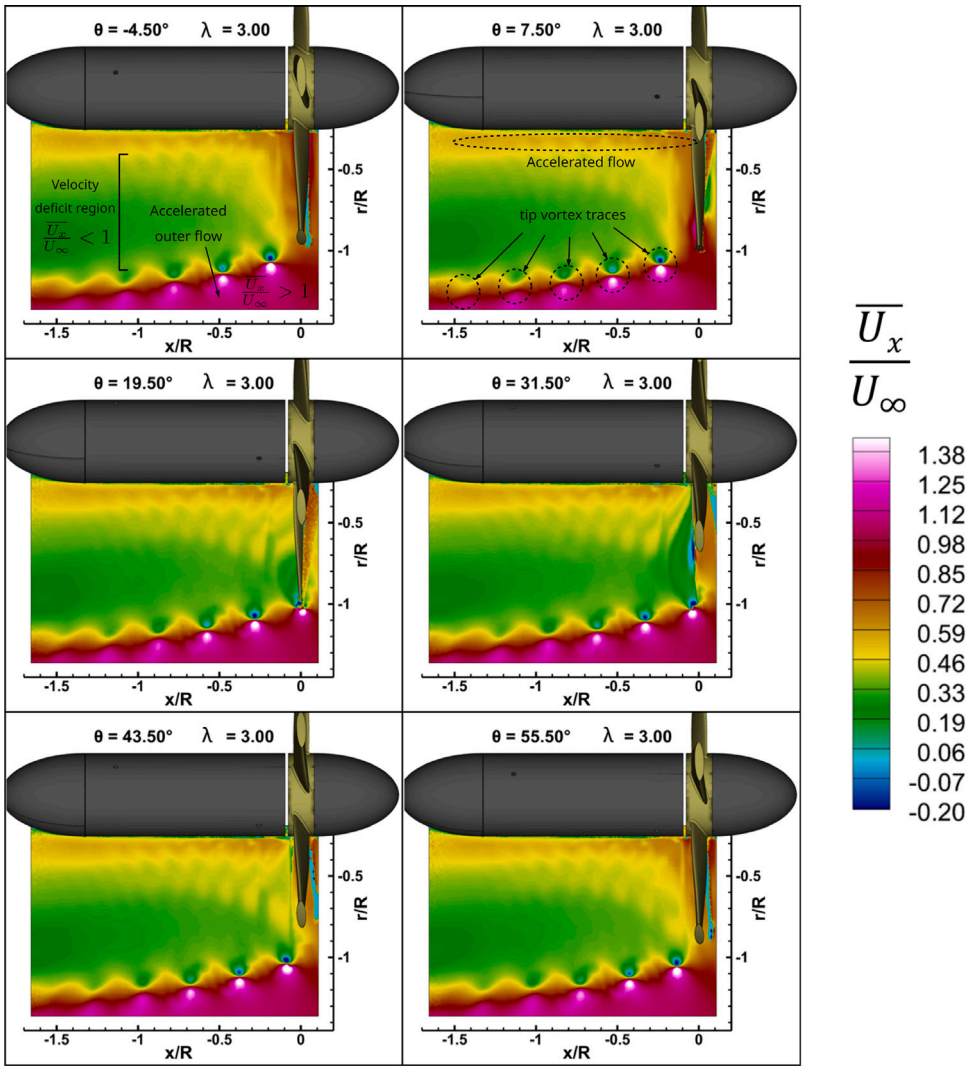

Fig. 7. Non-dimensional mean phase-locked axial velocity behind the turbine at $\lambda = 3.00$; see Video S1 for an animated sequence at other λ values and for varying θ.

$\overline{U_x}$ map. The shape is seen to evolve from a circular to a seemingly elliptically elongated shape in the downstream direction as shown in Fig. 9. However, this transformation is only apparent as the map is in fact the ensemble average of instantaneous vorticity maps, therefore it encases the random fluctuations of the tip vortex in space and time, known as vortex wandering. Correction approaches to address the effects of wandering on vortex measurements are available, see for instance [35], however none was applied here as the focus is on the turbulent content of the wake rather than on the detailed vortex characterization. The spatial instability is illustrated in Fig. 10 and the associated Video S4 where the instantaneous positions of the center of the tip vortex, defined as the location of the vorticity magnitude peak, are plotted as white markers. The peak is detected by tracking the maximum of the vorticity spots found in Fig. 9 at different instants, as in [36].

The map represents also the vorticity skewness $\mu_{\omega_\theta,3}$ in its normalized form, defined as $\mu_{\omega_\theta,3} = \overline{\omega_\theta'^3}/\sigma^3_{\omega_\theta}$, where $\omega'_\theta = \omega_\theta - \overline{\omega_\theta}$ with $\overline{\omega_\theta}$ being the mean of vorticity as per Eq. (2) and σ_{ω_θ} its standard deviation. The quantity $\mu_{\omega_\theta,3}$ is representative of the vortex spatial fluctuations and is therefore a measure of the level of asymmetry of the vorticity spots. The vortex cores are found to lay inside an area delimited by a markedly negative value of the vorticity skewness. This region represents the spatial extension of the tip vortex core's fluctuations within the axial–radial plane, and is seen to expand with increasing x/R. The fluctuations are not visible in Fig. 9 as a result of the low-pass nature of the averaging process. The vortex fluctuations are the first step toward the destabilization process of the helical vortex system released by the rotor and occurring further downstream [20,24].

The destabilization mechanism can be enhanced by the interaction between a tip vortex and the trailing edge wake released by the preceding blade. This blade-to-blade interaction is observed in the vorticity plots reported in Fig. 9 and is recognizable as a trailing wake being distorted by the flow entrainment between the two blades, see plot at $\theta = 55.5°$. In fact, the shear layer travels at a lower velocity with respect to the tip vortices and undergoes a gradual distortion and stretching in the longitudinal direction. This is particularly visible nearby the high-vorticity tip vortex cores, which capture and deform the trailing wakes. The process is well documented in the case of a propeller wake [36]. A higher number of blades cause these interactions to initiate closer to the rotor plane, eventually involving all the blade shear layers starting at $x/R < -1.00$.

3.3. Effect of tip speed ratio

Important modifications to the wake topology are observed when changing the operating condition of the turbine. We notice that a same power coefficient C_P can be reached both at low and high λ, see Fig. 6, however the corresponding flow dynamics are completely different. Figs. 11 and 12 show the mean axial and radial velocity components at

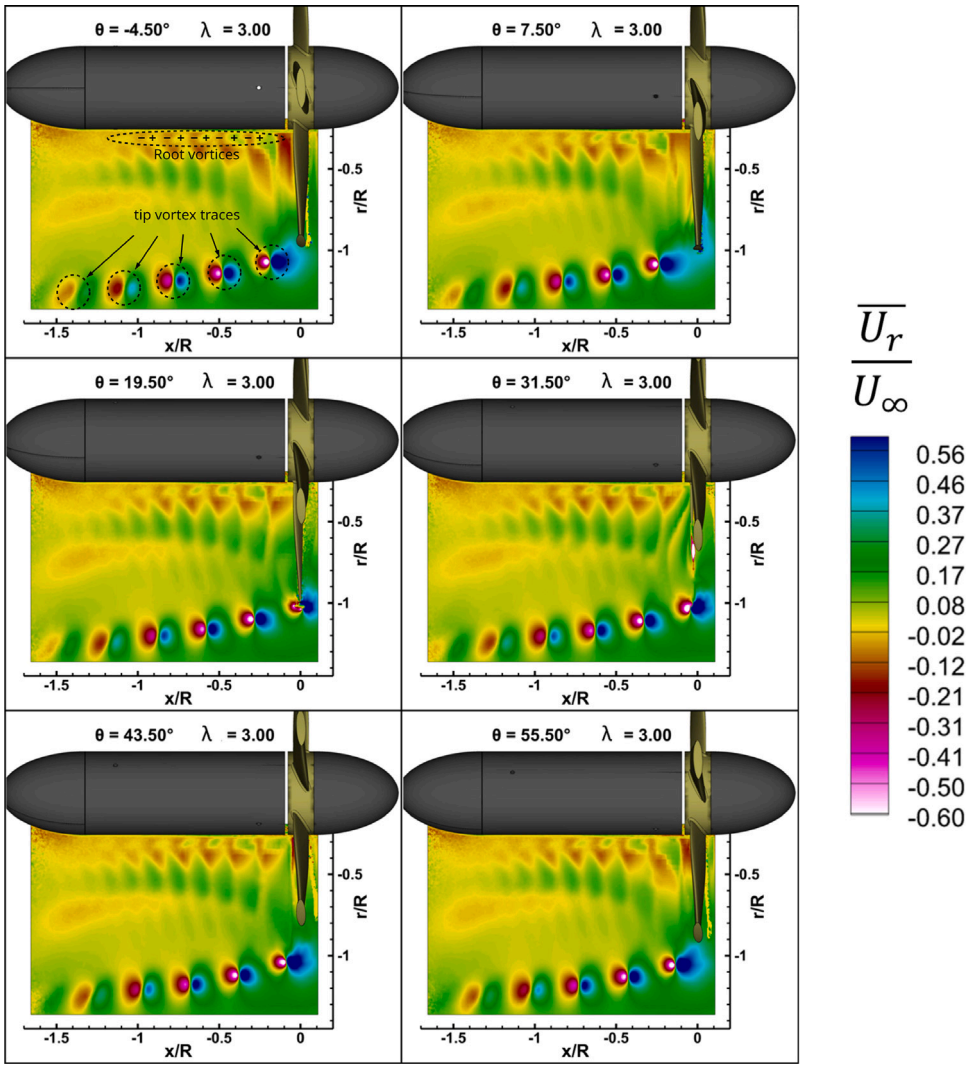

Fig. 8. Non-dimensional mean phase-locked radial velocity behind the turbine at $\lambda = 3.00$; see Video S2 for an animated sequence at other λ values and for varying θ.

different λ for a fixed rotor angle θ. At the lowest λ considered in this study ($\lambda = 0.60$), the rotor acts as an obstacle to the incoming flow, the kinetic energy of which is converted mostly into drag resistance. This is confirmed by the distribution of the velocity field, with the map of the axial velocity component indicating that the flow closer to the nacelle is strongly detached and can be even reversed, see Fig. 11 for λ comprised between 0.6 and 2.0. This large separation bubble extends in the radial direction up to $r/R \approx 0.7$ and changes topology as λ increases, stretching in the longitudinal direction and compacting in the radial one before disappearing as the turbine torque coefficient approaches its maximum at approximately $\lambda \approx 2.9$. Close to the point of maximum power coefficient, the axial velocity reduces to about 30% of the upstream velocity in the near-to-far wake in a region of x/R ranging approximately from -0.5 to -1, see map at $\lambda = 2.80$ in Fig. 11. This value is in agreement with the velocity limit of $\frac{1}{3}U_\infty$ expected at the maximum power coefficient, as predicted by the Betz elementary momentum theory based on the actuator disk [37]. The axial velocity behind the rotor increases with λ after the point of maximum power coefficient, especially in the inner part of the wake at smaller radii, as a result of the reduced capability of the turbine to extract energy from the flow with increasing λ. This situation corresponds to a progressive unloading of the turbine, which culminates at $\lambda = 6.5$ where most of the kinetic energy of the incoming flow passes through the rotor plane without being harvested, with $\overline{U_x}/U_\infty \gtrsim 80\%$.

The radial component shown in Fig. 12 puts into evidence the formation of a vortex at the tip starting at $\lambda > 1.2$, signaling the onset of lift production on the blade and consequently of higher torque and power output. As λ increases to the point of maximum power, the load on the blades induces stronger pressure gradients and consequently higher vorticity at the blade tip (see Video S3), until reaching the point of maximum C_P where the relative flow velocity is such that drag is minimized and lift is maximized.

The pitch of each tip vortex helix decreases with increasing λ as it follows the pressure gradient shift experienced between the low- and high-pressure faces of each blade. Beyond the point of maximum power, the distance reduces further as the tangential velocity increases and the pressure gradient moves upstream, while the vortices lose intensity and start to destabilize as unloading takes place. This is particularly evident in Fig. 13, which reports the distribution of the non-dimensional standard deviation σ_{U_x}/U_∞ of the axial velocity component U_x for different λ values. σ_{U_x} is defined as $\sqrt{\overline{u_x^2}}$ with $u_x = U - \overline{U_x}$ and is taken as a representative quantity of the turbulence intensity in the streamwise direction. We remark that the same considerations can be put forth with the radial component, not reported here for the sake of synthesis. The peak turbulence intensity is attained in the tip vortex core and results from the spatial fluctuations of this flow structure. The longitudinal distance between the second and third vortex cores is displayed, showing that it decreases monotonically with increasing λ. Note

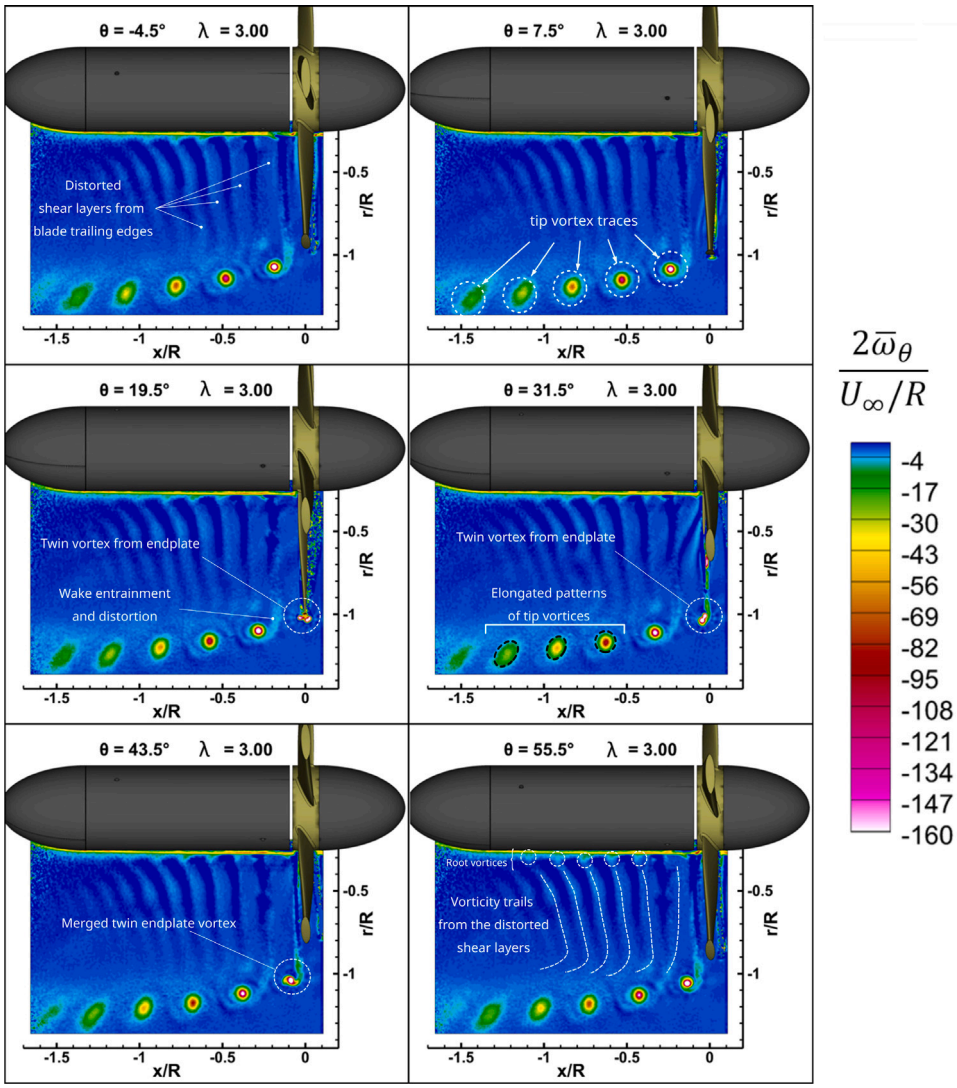

Fig. 9. Non-dimensional mean phase-locked vorticity behind the turbine at $\lambda = 3.00$; see Video S3 for an animated sequence at other λ values and for varying θ.

that the reported distance is in fact a fifth of the blade pitch. Starting at $\lambda \approx 3.80$ and $x/R < -1$, the tip vortex helices tend to interfere with each other, causing the turbulence intensity pattern around the vortex cores to spread by diffusion transport. The interference manifests itself as a pairing mechanism where two vortices start to roll-up in the so-called *leap-frog* behavior. Starting at $\lambda = 3.80$, this process is well visible on the θ-varying distribution of vorticity, see Video S3 or Video S5 (bottom right frame), as well as of the non-dimensional standard deviation σ_{U_r}/U_∞ of the radial velocity component U_r, see Video S6. At higher λ and at downstream locations $x/R < -1.0$, the interacting vortices merge into a single structure having a significantly larger footprint. Pairing and merging between vortices are the precursors to the breakdown of the vortical structures, after which the coherence of the rotor wake is lost.

The blade shear layer consists of small scale eddies and persists beyond $x/R < -0.3$ at all tip speed ratios λ, but quickly dissipates for $\lambda > 3.00$ as it evolves in the downstream direction with only a faint trace remaining. Therefore, the measurements show that the wake is primarily dominated by the evolution of the tip vortices, with the turbulence intensity being maximum in the tip vortex cores at the maximum C_P and in proximity of the rotor. Significant reduction of the turbulence levels through diffusion in the tip vortices is observed beyond the λ of maximum C_P. Finally, the distance between the root vortex helices is smaller than between the tip vortices because of the smaller angle of attack at the blade root, thus favoring their mutual interaction that combines with the nacelle boundary layer to promote a faster diffusion with respect to the tip vortices, see map at $\lambda = 2.80$ in Fig. 13.

3.4. Slipstream expansion

Downstream of the rotor the slipstream undergoes an expansion in which the pressure drop due to the mechanical work of the rotor is recovered. The expansion of the slipstream is evaluated by tracking the location of the peak of the mean vorticity at the tip vortex core from the data in Fig. 9. The results are shown in Fig. 14 at the different tip speed ratios λ up to a length of $\sim 1.6R$ in the downstream direction. The Betz theory predicts an expansion ratio of $\sqrt{2}R = 1.4$ at the maximum C_P while our measurements indicate an expansion ratio 7% lower of about 1.3 for $\lambda \approx 3.0$, albeit slightly beyond the point of maximum C_P. For λ below and above the maximum C_P, the expansion ratio is found to be lower. However, the slipstream radial expansion does not exhibit a monotonic behavior for $\lambda > 3.0$. This can also be observed on the map of the turbulence intensity reported in Fig. 13. At higher λ the vortex helices feature a reduced pitch as explained previously, and the distance between neighboring vortices decreases. This occurrence is associated to the onset of vortex interactions as reported in [24]:

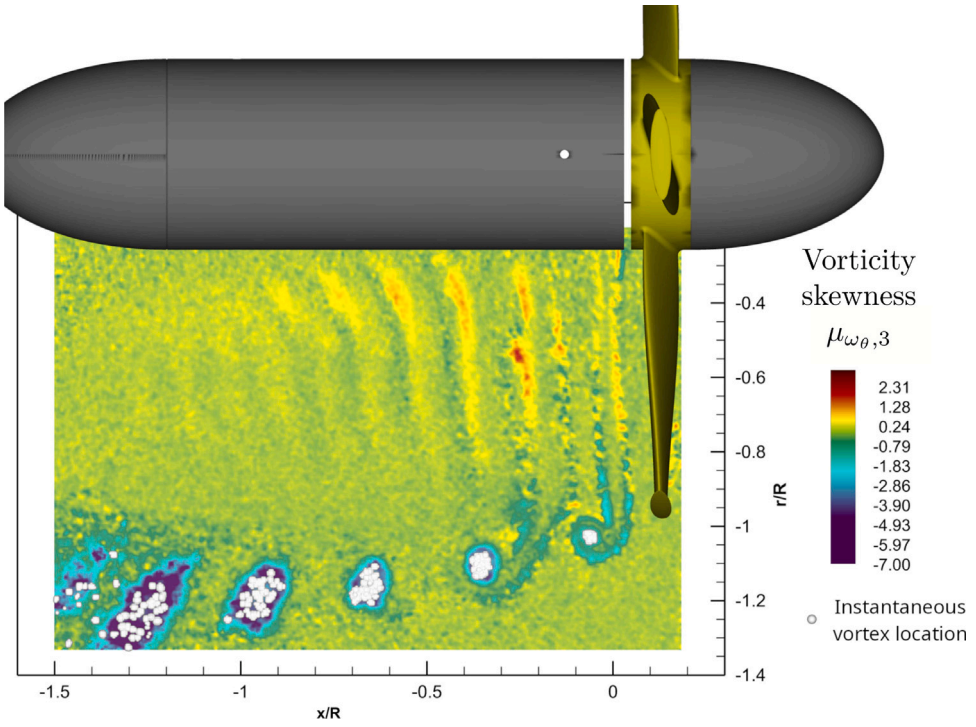

Fig. 10. Skewness of the in-plane vorticity, and tip vortex traces of 50 instantaneous measurements; see Video S4 for an animated sequence.

tip vortex helices start to pair triggering the instabilities of the vortex filaments released by the blades and their subsequent breakdown.

The rapid increase in the kinetic energy content within the wake has been reported to begin once the tip vortices have paired, and to complete approximately at 90°-rotation around their saddle points [23]. This location coincides with the onset of a three-dimensional breakdown of the helical vortices, which in turn induces a more efficient mixing in the wake, dominated by random fluctuations. This process is not fully captured in the present measurements as it occurs further downstream and outside of our observable domain. Nevertheless the initial phase of vortex pairing and subsequent breakdown is detected at the upper bound of the λ range, as per our comments upon Fig. 12. Fig. 15 reports the cross-term $\overline{u_x \cdot u_r}$ shown in non-dimensional form, where $u_x = U_x - \overline{U_x}$ and $u_r = U_r - \overline{U_r}$ are the fluctuating axial and radial components of the velocity field, respectively. Since the fluid density is considered constant, the cross-correlation term $\overline{u_x \cdot u_r}$ fully represents the Reynolds stresses. While the trace terms of the tensor are associated to the square of the axial and radial turbulence intensities σ_{U_x} (see Fig. 13) and σ_{U_r}, respectively, $\overline{u_x \cdot u_r}$ corresponds to the non-diagonal terms of the two-dimensional Reynolds stress tensor and represents the coupling between the normal components.

In the vortex core region, the $\overline{u_x \cdot u_r}$ cross-term of the Reynolds stress tensor typically features a structure with symmetrical side-lobes of alternate sign, which are representative of the velocity fluctuations of the vortex around its mean position. This pattern is clearly seen in Fig. 15 for $\lambda \geq 2.0$ when the wake gains coherence with the formation of the vortical system behind the rotor. This aspect can be better explained in the local moving reference system of a rigid vortex core moving downstream with the flow, as depicted in the schematic diagram shown in Fig. 16. In this model, the spatial fluctuations of the vortex cause a negative correlation of the term $\overline{u_x \cdot u_r}$ in the 1st and 3rd quadrants and a positive correlation in the 2nd and 4th quadrants. In a real situation, velocity gradients induce vortex dynamics such as stretching, twisting, tilting and bending, which affect the evolution of the Reynolds stress tensor. Fig. 16 also shows that $\overline{u_x \cdot u_r}$ is maximum when the fluctuations occur along the bisectors of these quadrants. To illustrate this behavior, the term $\overline{u_x \cdot u_r}$ as measured in the region surrounding the tip vortex is taken from Fig. 15 and displayed in Fig. 16 for the specific case of maximum power coefficient and at different downstream locations.

Fig. 16 shows that the vortex is fluctuating along two main directions perpendicular to each other in the useful working regime of the turbine, namely in the range $2.00 < \lambda < 3.00$. A comparison of the magnitude of $\overline{u_x \cdot u_r}$ in the side-lobes in the 1st and 3rd quadrant shows a relative increase whereas the magnitude in the 2nd and 4th quadrants vanishes to zero at $x/R = -0.96$. It can also be noted that the four-lobe structure of $\overline{u_x \cdot u_r}$ disappears at the onset of vortex pairing and destabilization as discussed upon Figs. 12 and 13, see graphical annotations in Fig. 15 as well as Video S7. In this case, the model described in Fig. 16 loses its applicability.

3.5. Turbulent kinetic energy

In this section several physical considerations are made in terms of the turbulent kinetic energy k. The kinetic energy of turbulence (TKE) can be written

$$k = \frac{1}{2}\overline{u_i\, u_i} \tag{3}$$

with subscript $i = 1, 2, 3$. The evolution of k in time and space is provided by the turbulent kinetic energy equation

$$\overline{\boldsymbol{U}} \cdot \nabla \left[\frac{1}{2}\overline{\boldsymbol{u}^2}\right] = \frac{\overline{D}}{Dt}k \qquad = -\nabla \cdot [\boldsymbol{T}] + \mathcal{P} - \varepsilon \tag{4}$$

where D is the material derivative and $\boldsymbol{T}$, $\mathcal{P}$ and ε are the transport tensor, production term and dissipation term, respectively. The notation $\overline{\boldsymbol{\Phi}}$, used throughout the text, indicates the mean of quantity $\boldsymbol{\Phi}$.

In tensor notation, Eq. (4) takes the form:

$$\overbrace{\frac{\overline{D}}{Dt}k}^{\frac{\overline{D}}{Dt}k} = \overbrace{-\nabla\cdot[\boldsymbol{T}]}^{\text{Transport}-\nabla\cdot[\boldsymbol{T}]} + \mathcal{P} - \varepsilon$$

$$\underbrace{\frac{\partial k}{\partial t}}_{\substack{\text{Local}\\ \text{derivative}}} + \underbrace{\overline{U_i}\frac{\partial k}{\partial x_i}}_{\substack{\text{Convective}\\ \text{transport}}} = \underbrace{-\frac{1}{\rho}\frac{\partial \overline{p\,u_j}}{\partial x_j}}_{\substack{\text{Pressure}\\ \text{diffusion}}} \underbrace{-\frac{1}{2}\frac{\partial \overline{u_i u_i u_j}}{\partial x_j}}_{\substack{\text{Turbulent}\\ \text{transport } \mathcal{T}}} + \underbrace{\nu\frac{\partial^2 k}{\partial x_j^2}}_{\substack{\text{Molecular viscous}\\ \text{transport } \mathcal{M}}}$$

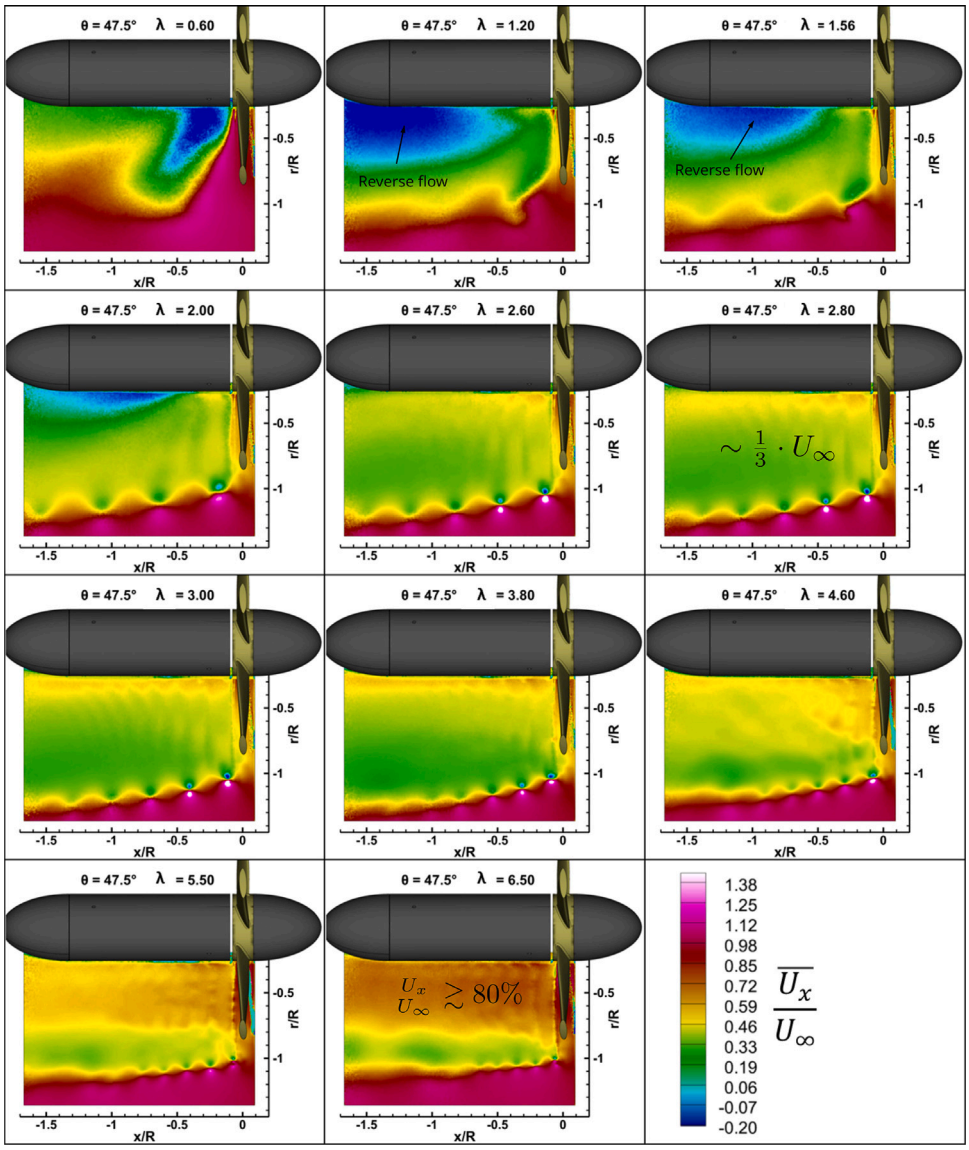

Fig. 11. Non-dimensional mean phase-locked axial velocity distribution behind the turbine at different operating conditions for the phase angle $\theta = 47.5°$; see Video S5 for an animated sequence at a fixed θ and for varying λ (top left frame).

$$\overbrace{-\overline{u_i u_j}\frac{\partial \overline{U_i}}{\partial x_j}}^{\text{Production } \mathcal{P}} \overbrace{-\nu\overline{\frac{\partial u_i}{\partial x_j}\frac{\partial u_i}{\partial x_j}}}^{\text{Dissipation } \varepsilon} \tag{5}$$

where $i, j = 1, 2, 3$ represent the vector components in the reference system of axes, and are in our case the axial, radial and tangential components, respectively; ν is the kinematic viscosity and R is the rotor radius. We will use the non-dimensional form of Eq. (5) using the following scaling transformations:

$$x_i^* \equiv \frac{x_i}{R}, \quad U_i^* \equiv \frac{U_i}{U_\infty}, \quad u_i^* \equiv \frac{u_i}{U_\infty}, \quad t^* \equiv t\frac{U_\infty}{R}, \quad p^* \equiv \frac{p}{\rho U_\infty^2}, \quad k^* \equiv \frac{k}{U_\infty^2}$$

Eq. (5) takes the following non-dimensional form, with R_e being the Reynolds number defined as $Re = U_\infty R/\nu$:

$$\frac{\partial k^*}{\partial t^*} + \overline{U_i^*}\frac{\partial k^*}{\partial x_i^*} = \underbrace{-\frac{\partial \overline{p^* u_j^*}}{\partial x_j^*}}_{\text{Pressure diffusion}} \underbrace{-\frac{1}{2}\frac{\partial \overline{u_i^* u_i^* u_j^*}}{\partial x_j^*}}_{\text{Turbulent transport } \mathcal{T}^*} + \underbrace{\frac{1}{R_e}\frac{\partial^2 k^*}{\partial x_j^{*2}}}_{\text{Molecular viscous transport } \mathcal{M}^*}$$

$$\underbrace{-\overline{u_i^* u_j^*}\frac{\partial \overline{U_i^*}}{\partial x_j^*}}_{\text{Production } \mathcal{P}^*} \underbrace{-\frac{1}{R_e}\overline{\frac{\partial u_i^*}{\partial x_j^*}\frac{\partial u_i^*}{\partial x_j^*}}}_{\text{Dissipation } \varepsilon^*} \tag{6}$$

The two-dimensional nature of the measurements limits the extent of the flow knowledge to two in-plane components, specifically the axial and radial vectors. Despite this constraint, insightful information can be obtained if we consider the order of magnitude of the different terms contributing to the turbulent kinetic energy. In fact, the missing information regarding the tangential velocity can be assumed to be of the same order of magnitude as the axial and radial one and will not change the relative weight of the different terms shown in Eq. (6), therefore this makes possible a comparison of the relative contribution of the terms $\mathcal{T}^*$, $\mathcal{P}^*$ and ε^* in the evolution of TKE. On the one hand, the terms on the right-hand side of Eq. (6) can be estimated with the present measurement dataset for $i, j \in [1, 2]$ with the exception of the pressure diffusion term, which is however in the order of magnitude of the turbulent transport term as per the Bernoulli equation, i.e. $p^* \propto u_i^* u_i^*$. On the other hand, the fact that the angular velocity $\omega = \dot{\theta}$ is constant makes possible to estimate the left-hand term $\left[\frac{\partial}{\partial t^*} + \overline{U_i^*}\frac{\partial}{\partial x_i^*}\right] k^*$

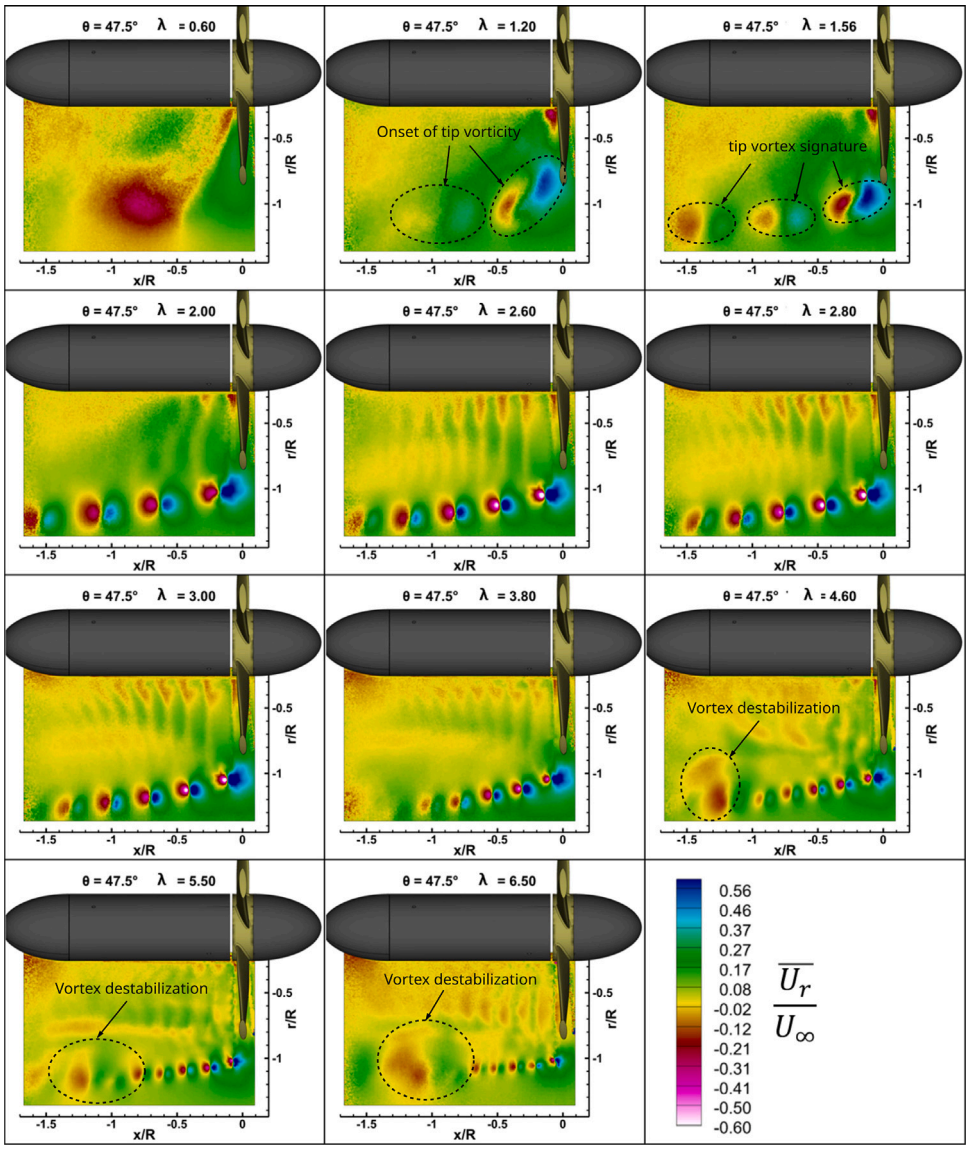

Fig. 12. Non-dimensional mean phase-locked radial velocity distribution behind the turbine at different operating conditions for the phase angle $\theta = 47.5°$; see Video S5 for an animated sequence at fixed θ and for varying λ (top right frame).

of Eq. (6) using the assumption of frozen flow in the angular direction and replacing the time derivative by the angular derivative in the axial and radial plane, such that $\frac{\partial}{\partial t} \equiv \dot{\theta}\frac{\partial}{\partial \theta}$.

The spatial distribution of the turbulent kinetic energy k^* in the wake for $\lambda = 3.0$ and $\theta = 0$ is shown in Fig. 17. High values of k^* are seen to be associated to the tip vortex cores. Significant turbulence levels linked to the shear layer at the blade trailing edge are also found at short axial distance from the rotor plane and expands across the radial direction, but dissipates rapidly further downstream.

The production term $\mathcal{P}^*$ and the transport term $\mathcal{T}^*$ are shown in Fig. 18, respectively on the left and right plots. These terms are largely dominant over the viscous effects in the downstream evolution of the turbulent kinetic energy, with magnitudes about two to three orders higher than those of the dissipation ϵ^* and four orders larger than the molecular viscous transport $\mathcal{M}^*$ shown in Fig. 19.

Figs. 20 and 21 show the evolution of the maximum of the turbulent kinetic energy k^* and dissipation term ϵ^*, respectively, as measured in the tip vortex core. Both are represented as a function of the axial distance x/R for all the phase angles and at a tip speed ratio $\lambda = 3.0$. As a further element to characterize the evolution of k^* and ϵ^*, we introduce the peak-to-width ratio for each of these two quantities. Assuming that the spots of k^* and ϵ^* seen in Figs. 17 and 19 have a non-isotropic Gaussian-like distribution, we define the peak width as the mean between the minor and major axes of the cross-sectional ellipse at half the peak magnitude. The peak-to-width ratio is then defined as the ratio between this latter value and the width hence defined, non-dimensionalized by the peak-to-width ratio measured at $x/R = 0$ and $\theta = 0°$. The quantity is reported on Figs. 20 and 21 on the right axes.

The turbulent kinetic energy is seen to increase in the range x/R from 0 to −0.6, and is explained by the interaction of the vortex cores with the wake originating from the trailing edge of the preceding blade. This is supported by the observations made upon the analysis of the vortex distribution, see Fig. 9 and the corresponding Video S3 showing the vorticity evolution during the rotation at different values of λ. The turbulent kinetic energy reaches a peak in proximity of the maximum expansion at $x/R \approx -0.75$, followed by a linear decay further downstream with a trend $dk^*/dx^* \approx 0.25$. The decay of k^* is minimally caused by the dissipation term ϵ^* of equation Eq. (6) since ϵ^* is one to two orders of magnitude lower with respect to the gradient of k^*, see Fig. 21. The decay of k^* is triggered by the diffusion processes, which are dominated by the turbulent transport term of Eq. (6) reported in Fig. 18. The broadening of the peak, observed in Fig. 20 in terms

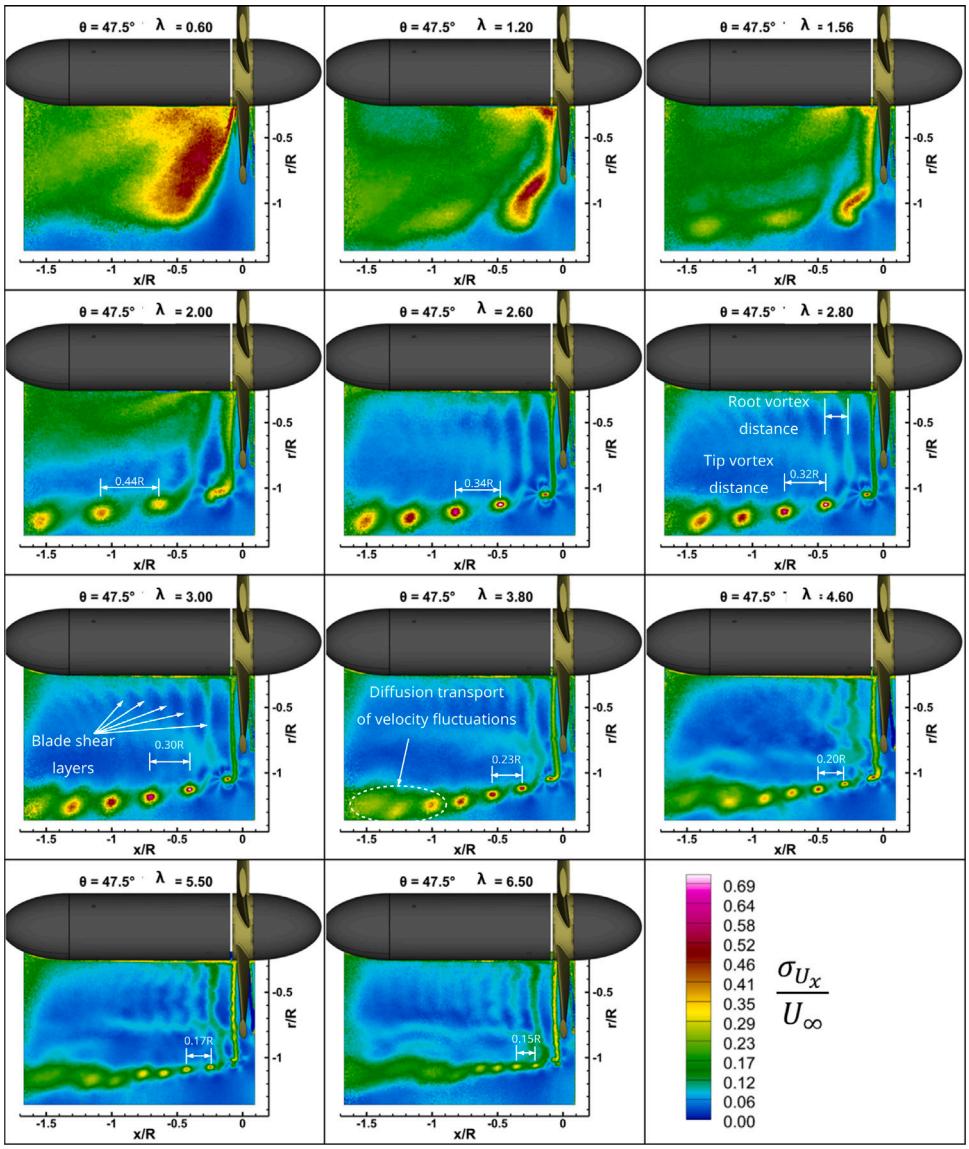

Fig. 13. Non-dimensional distribution of the standard deviation of the phase-locked axial velocity component behind the turbine at different operating conditions; see Video S5 for an animated sequence at fixed θ and for varying λ (bottom left frame), and Video S6 for an animated sequence of the associated σ_{U_r}/U_∞ quantity.

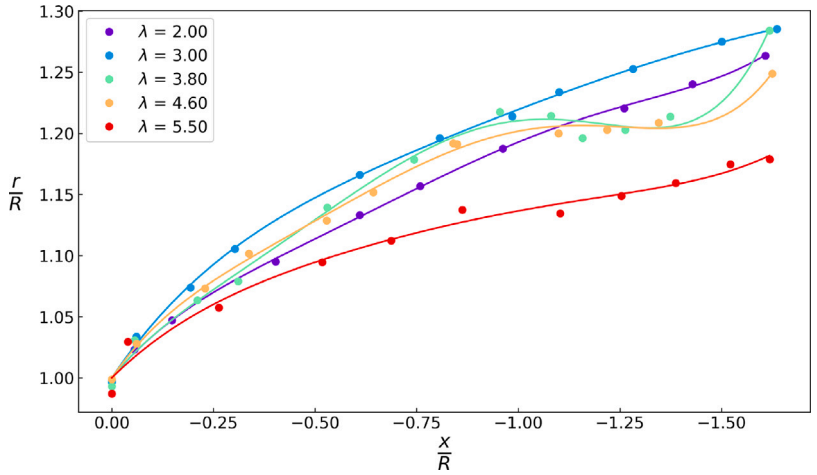

Fig. 14. Expansion ratio of the slipstream at five different operating conditions.

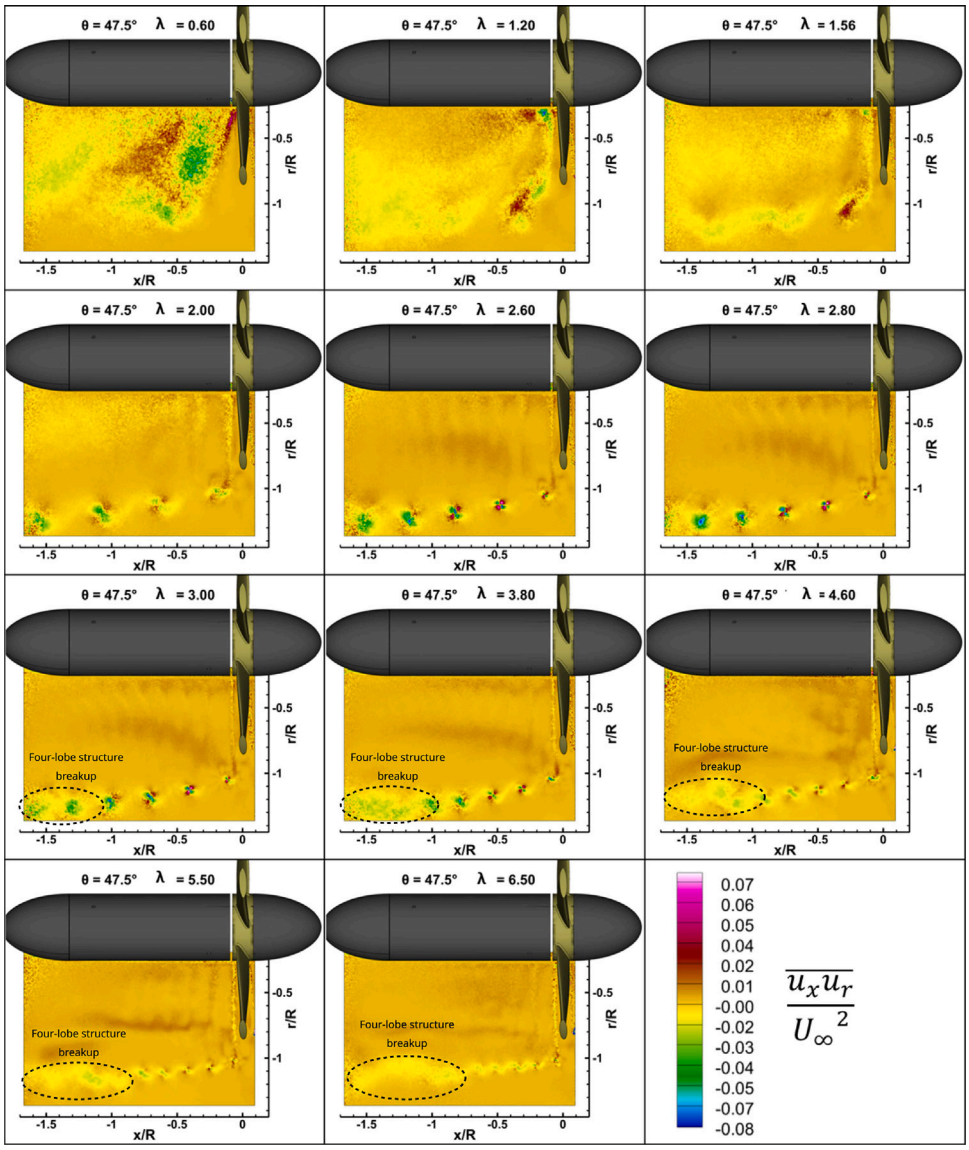

Fig. 15. Evolution of the non-diagonal term of the Reynolds stress tensor in the downstream direction for different operating conditions; see Video S7 for an animated sequence at varying θ.

of peak-to-width ratio, supports this observation. For $x/R < -1.3$ the dissipation increases as a consequence of the vortex pairing process that leads to vortex instabilities, further enhancing diffusion of the turbulent kinetic energy.

The pattern exhibited by $\mathcal{T}^*$ shows a strong similarity with the distribution of the cross-terms $\overline{u_i^* u_j^*}$ of the Reynolds stress tensor, see Figs. 15 and 16 and related discussion, suggesting that the transport and production terms are strongly correlated with the vortex fluctuations. In fact, as previously observed from Fig. 10, the spatial fluctuations of the tip vortex core are strongly correlated with the vorticity skewness coefficient as this quantity is shown to be directly linked to the triple correlations of the velocity fluctuations and therefore to the transport term of the turbulent kinetic energy.

Finally, the respective contributions of the production and transport terms $\mathcal{P}^*$ and $\mathcal{T}^*$ to the gradient of the turbulent kinetic energy k^* are pictured in Fig. 22. Here k^* is plotted as an elevation surface, which is then color-coded with the production and transport terms $\mathcal{P}^*$ and $\mathcal{T}^*$, respectively on the left and right plots. It appears that transport and production are clearly dominant in the regions of strong gradient of k^* and appear to act in opposition: in the region where the production is positive, hence a source of energy, the transport tends to be negative and acts as a sink of energy. Therefore, the principal mechanism driving the dynamics of the turbulent kinetic energy k^* is its transfer from the turbulent velocity components in the axial–radial plane to the tangential component and vice versa.

4. Conclusions

The spatial and temporal evolution of the wake of a tidal turbine was investigated at different operating conditions using the Particle Image Velocimetry (PIV) technique. Both instantaneous and averaged velocity fields were provided, phase-aligned with the angular position of the rotor blade. The experimental results, analyzed in terms of velocity, vorticity and turbulent kinetic energy, allow to identify and discriminate the different contributions to the hydrodynamics of the turbine wake and to its performance.

The analysis shows that a detached flow is formed behind the rotor and around the nacelle at low tip speed ratio λ. As λ increases, a blade tip vortex is generated as a result of the onset of lift and torque production. At the λ of maximum power coefficient C_P the intensity of the tip vortex and the radial expansion of the slipstream achieve their maximum amplitude; size of the slipstream and velocity in the wake are

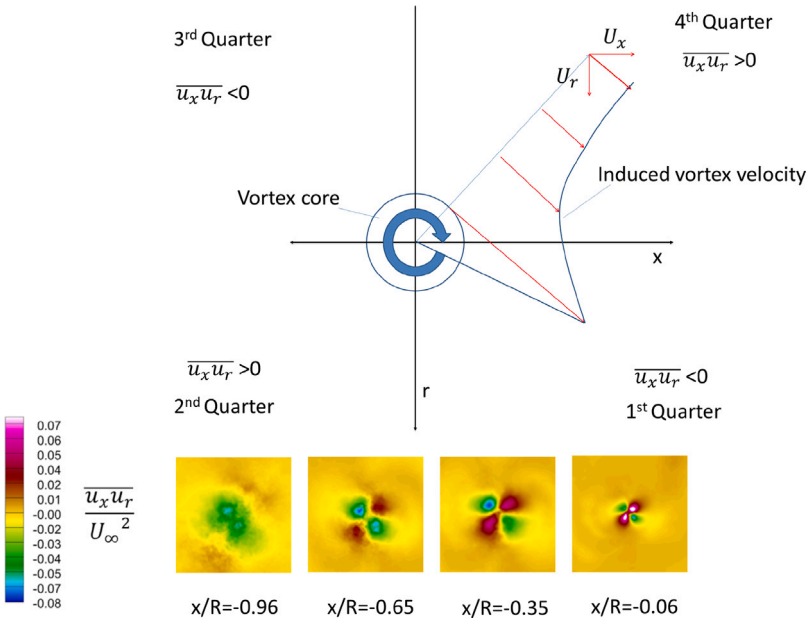

Fig. 16. Behavior of the non-diagonal term of the Reynolds stress tensor in the vortex core, and evolution at different locations in the downstream direction.

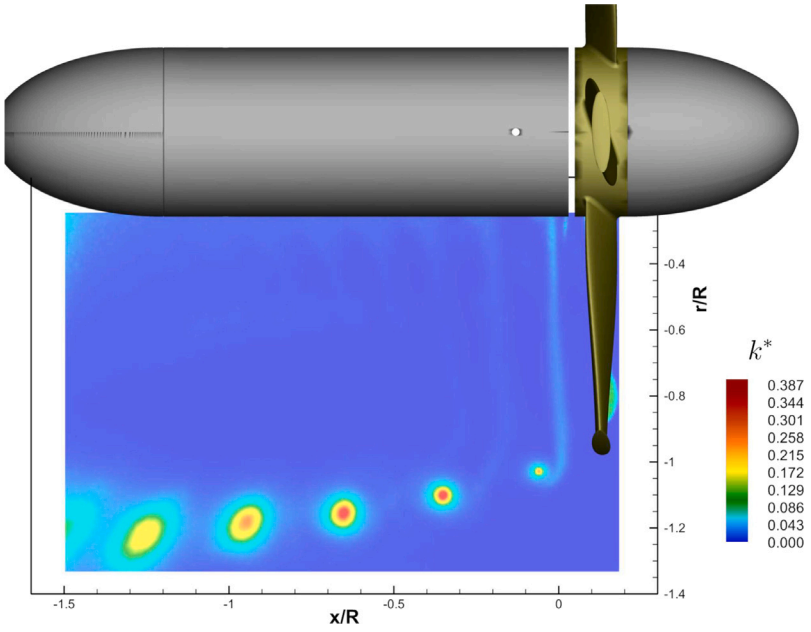

Fig. 17. Turbulent kinetic energy distribution behind the turbine at $\lambda = 3.00$ and $\theta = 0°$.

in close agreement with those predicted by the Betz theory. For higher λ both tend to reduce, while an increasing portion of the incoming flow kinetic energy passes unaffected through the rotor.

The non-diagonal terms of the Reynolds stress tensor are shown to be an effective sensor of the vortex instabilities, which indicate the onset of interaction mechanisms leading to tip vortex destabilization. It has been observed that the mechanism of blade-to-blade interaction is in fact the first perturbation triggering the tip vortex fluctuations eventually leading to its breakdown.

The distribution of the turbulent kinetic energy in the slipstream is dominated by the dynamics of the tip vortex. In this wake region the dissipation and viscous effects of the tip vortex are shown to have a minor influence. Beyond the point of maximum expansion at the λ of highest C_P, the peak of turbulent kinetic energy associated to the tip vortex cores is found to decay linearly in the downstream direction. The production and transport terms of the turbulent kinetic energy equation are energetically dominant over the dissipation processes. Both quantities appear to balance each other, suggesting a mechanism of energy transfer from the axial–radial plane to the tangential direction and vice versa. This mechanism is also clearly expressed through the vorticity skewness, which quantifies the vortex fluctuations and is indeed related to the triple velocity correlations of the transport term.

The findings presented in this study provide a detailed insight into the hydrodynamics of a tidal current turbine. The results suggest that the experimental approach used here could be implemented as an efficient tool to improve to design and operation of tidal turbines. Specifically, such a tool could be beneficial to achieve a better control of the wake stability and consequently optimize the re-energizing potential of the wake. Furthermore the results are important as an input for the validation of advanced flow computations where turbulence can

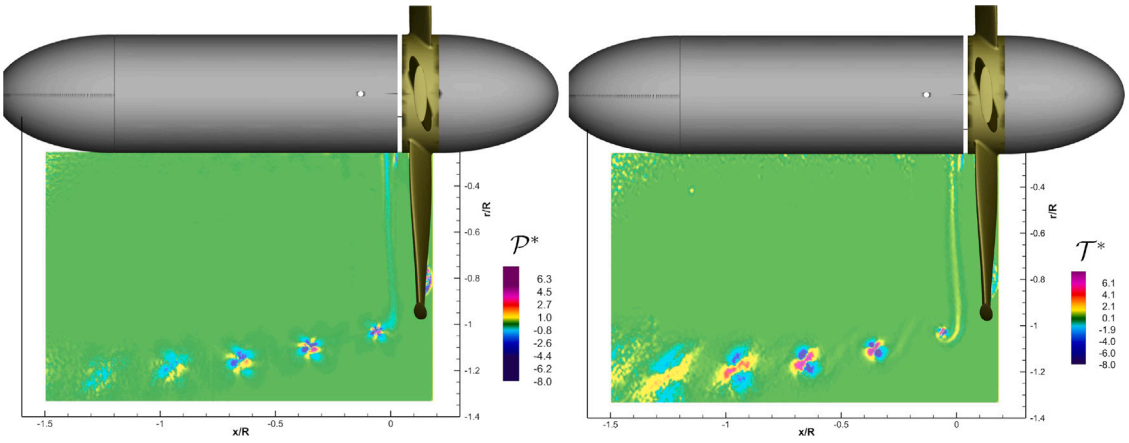

Fig. 18. Longitudinal evolution of the production term $\mathcal{P}^*$ and transport term $\mathcal{T}^*$ of the turbulent kinetic energy at $\lambda = 3.00$ and $\theta = 0°$.

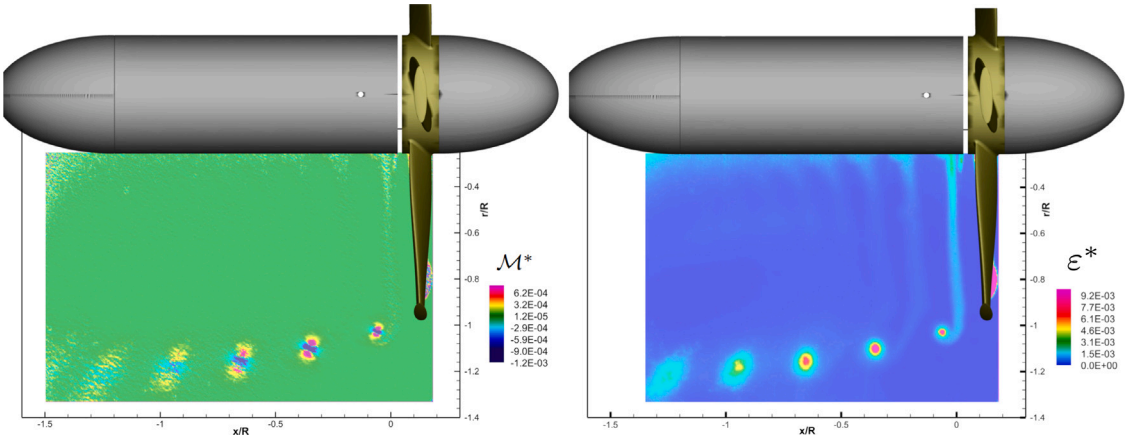

Fig. 19. Longitudinal evolution of the molecular viscous transport term $\mathcal{M}^*$ and dissipation term ε^* of the turbulent kinetic energy at $\lambda = 3.00$ and $\theta = 0°$.

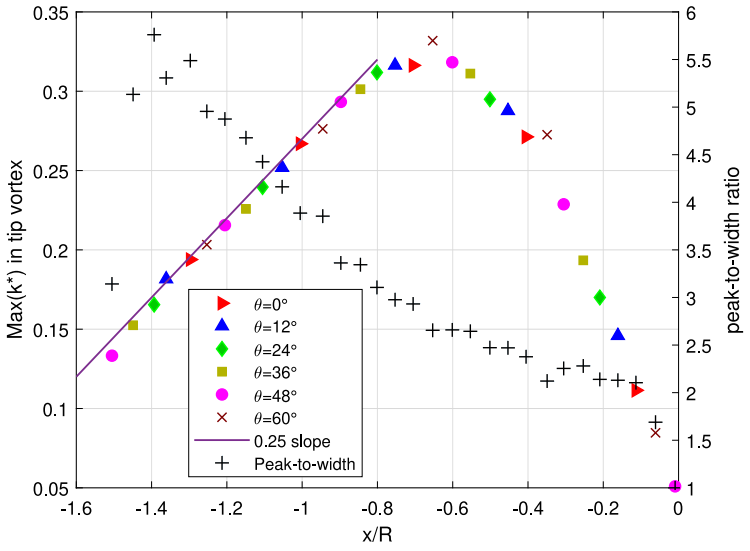

Fig. 20. Downstream evolution of the turbulent kinetic energy k^* in the vortex core at $\lambda = 3.00$: turbulent kinetic energy peak and peak-to-width ratio, respectively on the left and right coordinate axes.

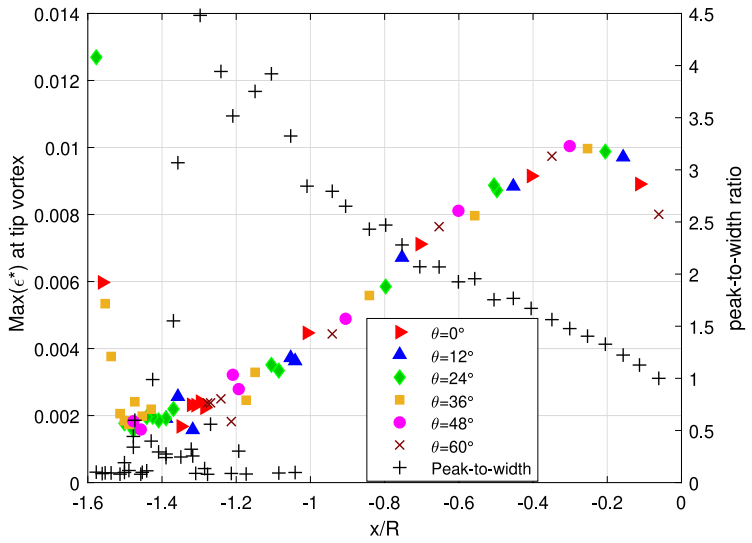

Fig. 21. Downstream evolution of the dissipation ϵ^* in the vortex core at $\lambda = 3.00$: dissipation peak and peak-to-width ratio, respectively on the left and right coordinate axes.

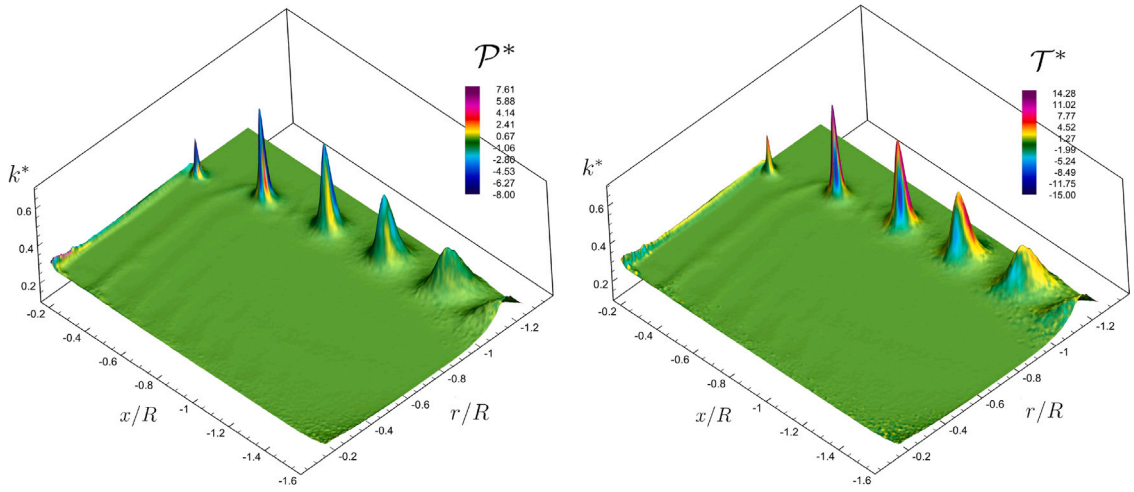

Fig. 22. Longitudinal evolution of k^* color-coded with the production term $\mathcal{P}^*$ (left) and the transport term $\mathcal{T}^*$ (right).

be resolved in detail. As such, the experimental approach and analysis deployed here could be part of the design process of future tidal current turbine farms.

CRediT authorship contribution statement

Fabio Di Felice: Conceptualization, Methodology, Software, Formal analysis, Investigation, Data curation, Writing – original draft, Writing – review & editing, Visualization, Supervision, Project administration, Funding acquisition. **Alessandro Capone:** Writing – review & editing. **Giovanni Paolo Romano:** Writing – review & editing. **Francisco Alves Pereira:** Conceptualization, Methodology, Software, Formal analysis, Investigation, Data curation, Writing – original draft, Writing – review & editing, Visualization, Supervision.

Declaration of competing interest

The authors declare that they have no known competing financial interests or personal relationships that could have appeared to influence the work reported in this paper.

Acknowledgments

The work was funded and performed under the EU-FP7 project MARINET, European Union (EU), grant agreement number 262552. The authors thank the CNR-INM Circulating Water Channel technical staff. The Authors are also thankful to C. Del Frate who contributed to the experimental and analysis work as part of her master thesis.

Appendix A. Supplementary data

Supplementary material related to this article can be found online at https://doi.org/10.1016/j.renene.2023.04.128.

References

[1] A. Hansen, C. Butterfield, Aerodynamics of horizontal-axis wind turbines, Annu. Rev. Fluid Mech. 25 (1) (1993) 115–149, http://dx.doi.org/10.1146/annurev.fl.25.010193.000555.

[2] T. Blackmore, L.E. Myers, A.S. Bahaj, Effects of turbulence on tidal turbines: Implications to performance, blade loads, and condition monitoring, Int. J. Mar. Energy 14 (2016) 1–26, http://dx.doi.org/10.1016/j.ijome.2016.04.017.

[3] P. Mycek, B. Gaurier, G. Germain, G. Pinon, E. Rivoalen, Experimental study of the turbulence intensity effects on marine current turbines behaviour. Part II: Two interacting turbines, Renew. Energy 68 (2014) 876–892, http://dx.doi.org/10.1016/j.renene.2013.12.048.
[4] A. Bahaj, A. Molland, J. Chaplin, W. Batten, Power and thrust measurements of marine current turbines under various hydrodynamic flow conditions in a cavitation tunnel and a towing tank, Renew. Energy 32 (3) (2007) 407–426, http://dx.doi.org/10.1016/j.renene.2006.01.012.
[5] P. Mycek, B. Gaurier, G. Germain, G. Pinon, E. Rivoalen, Experimental study of the turbulence intensity effects on marine current turbines behaviour. Part I: One single turbine, Renew. Energy 66 (2014) 729–746, http://dx.doi.org/10.1016/j.renene.2013.12.036.
[6] L. Myers, A. Bahaj, Wake studies of a 1/30th scale horizontal axis marine current turbine, Ocean Eng. 34 (5–6) (2007) 758–762, http://dx.doi.org/10.1016/j.oceaneng.2006.04.013.
[7] F. Maganga, G. Germain, J. King, G. Pinon, E. Rivoalen, Experimental characterisation of flow effects on marine current turbine behaviour and on its wake properties, IET Renew. Power Gener. 4 (6) (2010) 498–509, http://dx.doi.org/10.1049/iet-rpg.2009.0205.
[8] A.S. Bahaj, L.E. Myers, R.I. Rawlinson-Smith, M. Thomson, The effect of boundary proximity upon the wake structure of horizontal axis marine current turbines, J. Offshore Mech. Arct. Eng. 134 (2) (2011) 021104, http://dx.doi.org/10.1115/1.4004523.
[9] L. Chamorro, C. Hill, S. Morton, C. Ellis, R. Arndt, F. Sotiropoulos, On the interaction between a turbulent open channel flow and an axial-flow turbine, J. Fluid Mech. 716 (2013) 658, http://dx.doi.org/10.1017/jfm.2012.571.
[10] V.S. Neary, B. Gunawan, C. Hill, L.P. Chamorro, Near and far field flow disturbances induced by model hydrokinetic turbine: ADV and ADP comparison, Renew. Energy 60 (2013) 1–6, http://dx.doi.org/10.1016/j.renene.2013.03.030.
[11] B. Morandi, F. Di Felice, M. Costanzo, G.P. Romano, D. Dhomé, J.-C. Allo, Experimental investigation of the near wake of a horizontal axis tidal current turbine, Int. J. Mar. Energy 14 (2016) 229–247, http://dx.doi.org/10.1016/j.ijome.2016.02.004.
[12] Y. Chen, B. Lin, J. Lin, S. Wang, Experimental study of wake structure behind a horizontal axis tidal stream turbine, Appl. Energy 196 (2017) 82–96, http://dx.doi.org/10.1016/j.apenergy.2017.03.126.
[13] J. Lee, Y. Kim, A. Khosronejad, S. Kang, Experimental study of the wake characteristics of an axial flow hydrokinetic turbine at different tip speed ratios, Ocean Eng. 196 (2020) 106777, http://dx.doi.org/10.1016/j.oceaneng.2019.106777.
[14] Y. Zhang, Z. Zhang, J. Zheng, J. Zhang, Y. Zheng, W. Zang, X. Lin, E. Fernandez-Rodriguez, Experimental investigation into effects of boundary proximity and blockage on horizontal-axis tidal turbine wake, Ocean Eng. 225 (2021) 108829, http://dx.doi.org/10.1016/j.oceaneng.2021.108829.
[15] S. Kang, I. Borazjani, J.A. Colby, F. Sotiropoulos, Numerical simulation of 3D flow past a real-life marine hydrokinetic turbine, Adv. Water Resour. 39 (2012) 33–43, http://dx.doi.org/10.1016/j.advwatres.2011.12.012.
[16] S. Ke, W. Wen-Quan, Y. Yan, The hydrodynamic performance of a tidal-stream turbine in shear flow, Ocean Eng. 199 (2020) 107035, http://dx.doi.org/10.1016/j.oceaneng.2020.107035.
[17] D. Gajardo, C. Escauriaza, D.M. Ingram, Capturing the development and interactions of wakes in tidal turbine arrays using a coupled BEM-des model, Ocean Eng. 181 (2019) 71–88, http://dx.doi.org/10.1016/j.oceaneng.2019.03.064.
[18] S. Chawdhary, C. Hill, X. Yang, M. Guala, D. Corren, J. Colby, F. Sotiropoulos, Wake characteristics of a TriFrame of axial-flow hydrokinetic turbines, Renew. Energy 109 (2017) 332–345, http://dx.doi.org/10.1016/j.renene.2017.03.029.
[19] M. Nuernberg, L. Tao, Experimental study of wake characteristics in tidal turbine arrays, Renew. Energy 127 (2018) 168–181, http://dx.doi.org/10.1016/j.renene.2018.04.053.
[20] G.V. Iungo, F. Viola, S. Camarri, F. Porté-Agel, F. Gallaire, Linear stability analysis of wind turbine wakes performed on wind tunnel measurements, J. Fluid Mech. 737 (2013) 499–526, http://dx.doi.org/10.1017/jfm.2013.569.
[21] I.V. Naumov, R.F. Mikkelsen, V.L. Okulov, J.N. Sørensen, PIV and LDA measurements of the wake behind a wind turbine model, J. Phys. Conf. Ser. 524 (2014) 012168, http://dx.doi.org/10.1088/1742-6596/524/1/012168.
[22] S.C. Tedds, I. Owen, R.J. Poole, Near-wake characteristics of a model horizontal axis tidal stream turbine, Renew. Energy 63 (2014) 222–235, http://dx.doi.org/10.1016/j.renene.2013.09.011.
[23] L.E.M. Lignarolo, D. Ragni, C. Krishnaswami, Q. Chen, C.J.S. [Ferreira], G.J.W. [van Bussel], Experimental analysis of the wake of a horizontal-axis wind-turbine model, Renew. Energy 70 (2014) 31–46, http://dx.doi.org/10.1016/j.renene.2014.01.020, Special issue on aerodynamics of offshore wind energy systems and wakes.
[24] L. Lignarolo, D. Ragni, F. Scarano, C. Simão Ferreira, G. van Bussel, Tip-vortex instability and turbulent mixing in wind-turbine wakes, J. Fluid Mech. 781 (2015) 467–493, http://dx.doi.org/10.1017/jfm.2015.470.
[25] R.J. Barthelmie, S.T. Frandsen, M.N. Nielsen, S.C. Pryor, P.-E. Rethore, H.E. Jørgensen, Modelling and measurements of power losses and turbulence intensity in wind turbine wakes at Middelgrunden offshore wind farm, Wind Energy 10 (6) (2007) 517–528, http://dx.doi.org/10.1002/we.238.
[26] J. Whale, C.G. Anderson, R. Bareiss, S. Wagner, An experimental and numerical study of the vortex structure in the wake of a wind turbine, J. Wind Eng. Ind. Aerodyn. 84 (1) (2000) 1–21, http://dx.doi.org/10.1016/s0167-6105(98)00201-3.
[27] I. Grant, M. Mo, X. Pan, P. Parkin, J. Powell, H. Reinecke, K. Shuang, F. Coton, D. Lee, An experimental and numerical study of the vortex filaments in the wake of an operational, horizontal-axis, wind turbine, J. Wind Eng. Ind. Aerodyn. 85 (2) (2000) 177–189, http://dx.doi.org/10.1016/s0167-6105(99)00139-7.
[28] F. Massouh, I. Dobrev, Exploration of the vortex wake behind of wind turbine rotor, J. Phys. Conf. Ser. 75 (2007) 012036, http://dx.doi.org/10.1088/1742-6596/75/1/012036.
[29] R.J. Adrian, J. Westerweel, Particle Image Velocimetry, Cambridge University Press, Cambridge, New York, 2011.
[30] A. Melling, Tracer particles and seeding for particle image velocimetry, Meas. Sci. Technol. 8 (12) (1997) 1406–1416, http://dx.doi.org/10.1088/0957-0233/8/12/005.
[31] D. Di Florio, F. Di Felice, G.P. Romano, Windowing, re-shaping and re-orientation interrogation windows in particle image velocimetry for the investigation of shear flows, Meas. Sci. Technol. 13 (7) (2002) 953–962, http://dx.doi.org/10.1088/0957-0233/13/7/301.
[32] A.K.M.F. Hussain, W.C. Reynolds, The mechanics of an organized wave in turbulent shear flow, J. Fluid Mech. 41 (2) (1970) 241–258, http://dx.doi.org/10.1017/s0022112070000605.
[33] P. Jeffcoate, F. Salvatore, B. Boake, C. Elsaesser, Effect of submergence on tidal turbine performance, in: Proceedings of the 11th European Wave and Tidal Energy Conference, EWTEC 2015, Nantes, France, 2015, pp. 1–7.
[34] J. Yan, X. Deng, A. Korobenko, Y. Bazilevs, Free-surface flow modeling and simulation of horizontal-axis tidal-stream turbines, Comput. & Fluids 158 (2017) 157–166, http://dx.doi.org/10.1016/j.compfluid.2016.06.016.
[35] M. Dreyer, J. Decaix, C. Münch-Alligné, M. Farhat, Mind the gap: a new insight into the tip leakage vortex using stereo-PIV, Exp. Fluids 55 (11) (2014) http://dx.doi.org/10.1007/s00348-014-1849-7.
[36] A. Cotroni, F.D. Felice, G.P. Romano, M. Elefante, Investigation of the near wake of a propeller using particle image velocimetry, Exp. Fluids 29 (7) (2000) S227–S236, http://dx.doi.org/10.1007/s003480070025.
[37] A. Betz, Wind-driven rotors, in: A. Betz (Ed.), Introduction to the Theory of Flow Machines, Pergamon, 1966, pp. 236–241, http://dx.doi.org/10.1016/B978-0-08-011433-0.50070-9.